Received: 1 March 2019 | Revised: 27 June 2019 | Accepted: 25 July 2019

DOI: 10.1002/cnm.3246

SPECIAL ISSUE ARTICLE

WILEY

Impact of baseline coronary flow and its distribution on fractional flow reserve prediction

Lucas O. Müller[1] | Fredrik E. Fossan[1] | Anders T. Bråten[2,4] | Arve Jørgensen[3,4] | Rune Wiseth[2,4] | Leif R. Hellevik[1]

[1] Department of Structural Engineering, Norwegian University of Science and Technology, Trondheim, Norway

[2] Clinic of Cardiology, St. Olavs Hospital, Trondheim, Norway

[3] Department of Radiology and Nuclear Medicine, St. Olavs Hospital, Trondheim, Norway

[4] Department of Circulation and Medical Imaging, Norwegian University of Science and Technology, Trondheim, Norway

Correspondence
Fredrik E. Fossan, Department of Structural Engineering, Norwegian University of Science and Technology, Trondheim, Norway.
Email: fredrik.e.fossan@ntnu.no

Present Address
Frederik E. Fossan, Richard Birkelands, vei 1A,7491 Trondheim, Norway

Abstract

Model-based prediction of fractional flow reserve (FFR) in the context of stable coronary artery disease (CAD) diagnosis requires a number of modelling assumptions. One of these assumptions is the definition of a baseline coronary flow, ie, total coronary flow at rest prior to the administration of drugs needed to perform invasive measurements. Here we explore the impact of several methods available in the literature to estimate and distribute baseline coronary flow on FFR predictions obtained with a reduced-order model. We consider 63 patients with suspected stable CAD, for a total of 105 invasive FFR measurements. First, we improve a reduced-order model with respect to previous results and validate its performance versus results obtained with a 3D model. Next, we assess the impact of a wide range of methods to impose and distribute baseline coronary flow on FFR prediction, which proved to have a significant impact on diagnostic performance. However, none of the proposed methods resulted in a significant improvement of prediction error standard deviation. Finally, we show that intrinsic uncertainties related to stenosis geometry and the effect of hyperemic inducing drugs have to be addressed in order to improve FFR prediction accuracy.

KEYWORDS

coronary flow, fractional flow reserve, reduced-order model

Abbreviations: CAD, coronary artery disease; CCTA, coronary computed tomography angiography; CO, cardiac output; DBP, diastolic blood pressure; DM, distal murray; FFR, fractional flow reserve; HR, heart rateY age; HU, houndsfield units; ICA, invasive coronary angiography; LAD, left anterior descending; LCX, left circumflex; LM, left main; LVM, left ventricle mass; MAP, mean arterial pressure; PCI, percutaneous coronary intervention; PM, proximal murray; PP, pulse pressure; QCA, quantitative coronary angiography; RCA, right coronary artery; RPDA, right posterior descending artery; SBP, systolic blood pressure; SD, stenosis degree; SV, stroke volume; TAG, transluminal attenuation gradient; TMM, total myocardial mass; US, ultrasound; W, weight.

1 | INTRODUCTION

Fractional flow reserve (FFR) is an index to characterise the functional significance of coronary artery stenoses.[1,2] Although FFR is computed as the ratio between invasively measured post-stenotic and central aortic pressures, this index was originally derived to represent the ratio between the actual transtenotic flow over the hypothetical flow that would be observed in the absence of the stenosis under examination.[3] The theoretical derivation of FFR assumes constant peripheral resistance, which in turn is considered to be achieved under maximal vasodilation.[3] As a consequence, FFR is measured in hyperemic conditions, normally caused by the administration of a drug, such as adenosine, that selectively vasodilates the coronary peripheral vasculature.[4] A key advantage of FFR over more conventional methods, such as quantitative coronary angiography (QCA), is that, in addition to taking into account the geometry of a given lesion, it implies considering information about flow (under hyperemic conditions). In fact, after having been tested in large trials,[5-7] FFR is nowadays recommended to guide revascularization strategy in patients with stable coronary artery disease (CAD) without evidence of ischemia in non-invasive testing.[8] In practice, if a lesion is below a certain threshold, $FFR \leq FFR_{threshold}$, with $FFR_{threshold}=0.8$, the recommendation is to intervene by performing percutaneous coronary intervention (PCI) or in some instances bypass surgery, while a negative outcome, ie, $FFR>FFR_{threshold}$, results in treating the patient with optimal medical therapy.[8] Besides the proven validity of FFR as a a tool for functional assessment of stenosis severity, it remains an invasive procedure with associated risks. Moreover, in a study comprising almost 400 000 patients with suspected CAD from 663 US hospitals, almost two-thirds of the patients who underwent elective cardiac catheterisation proved to have non-obstructive CAD as determined by invasive angiography.[9] These considerations have motivated the search for non-invasive tests to reduce the number of invasive procedures. One of the most promising methods so far is coronary computed tomography angiography (CCTA). CCTA is a non-invasive anatomical imaging modality that allows to quantify the geometrical significance of a lesion and has a high diagnostic accuracy when compared with invasive coronary angiography-based diagnosis. A recent randomised trial suggested that CCTA improves patient outcome compared with standard care,[10] and guidelines currently suggest considering CCTA as a first-line test in all patients with suspected stable CAD.[11] CCTA has shown to be very selective in terms of correctly identifying CAD ($FFR \leq FFR_{threshold}$), while its performance to exclude CAD ($FFR>FFR_{threshold}$) is not as satisfactory, resulting in many false positive recommendations, ie, many patients undergo an invasive procedure for FFR measurement that could have been avoided if a more selective non-invasive method would have been used.[12]

In this scenario, CCTA-derived FFR has emerged as a possible response to the need for reducing false positive CCTA recommendations. Over the last decade, a significant number of methods for non-invasive computation of FFR based on CCTA have been proposed.[13] Such methods aim at predicting FFR for a given patient by using non-invasive information only and have already shown potential to be used as a screening tool on top of CCTA assessment.[14] These methods, based on reproducing the fluid mechanics in coronary vessels, share some common general steps that must be followed to deliver FFR predictions: (i) define the computational domain of coronary vessels; (ii) define a mathematical model for fluid mechanics valid in the domain defined in (i); (iii) define boundary conditions; (iv) solve the mathematical model; and (v) evaluate predicted FFR at desired locations. Although such steps can be found in any model-based FFR prediction method, the way in which each of these steps is performed varies greatly. In this paper, we address two aspects of this pipeline. First, we consider steps (ii) and (iv), working on the improvement and validation of a reduced-order model for the coronary circulation that allows for fast and accurate FFR prediction. Then, we focus on step (iii), investigating the impact of several methods for baseline coronary flow estimation and flow distribution proposed so far in the literature on FFR prediction.

Step (ii) of the general modelling strategy defined above requires making a choice on the mathematical model to be used for describing blood flow in coronary arteries. While in principle, many options are available, the most frequent choices found in the literature are 3D incompressible Navier-Stokes in rigid domains and 1D blood flow models in deformable vessels or fully lumped-parameter models. In general, 1D or lumped-parameter models are called reduced-order models. Several reduced-order models for FFR prediction have been proposed previously.[15-19] However, validation by comparison of predicted FFR with respect to results obtained by using more complex models was undertaken only in.[17-19] In Boileau et al,[18] a virtual population constructed from a single patient was used, while in Blanco et al,[17] a population of 20 patients was considered. Here, we modify the method proposed in Fossan et al[19] and validate it on a set of 63 patients (105 FFR measurements). For each patient, we perform simulations using a 3D model for the coronary vessels' domain and use those results as reference. To the best of our knowledge, such an extensive validation of the capacity of a reduced-order model to reproduce fluid mechanical aspects of model-based FFR prediction has not been performed so far.

The definition of boundary conditions for model-based FFR prediction is an unavoidable step. The sensitivity of predicted FFR to these boundary conditions was explored in previous studies[19-21] and was shown to be extremely relevant. In particular, Fossan et al[19] and Morris et al[21] showed that parameters that determine the hyperemic coronary flow have the highest influence on predicted FFR, for realistic ranges of other parameters. Motivated by this fact, we consider two aspects related to the definition of coronary flow, namely, baseline coronary flow and its distribution among the vessels of the network. In fact, virtually all methods for FFR prediction proposed so far require a baseline flow to be imposed and a criterion to distribute it among vessels in the network. Here, we have selected a set of representative methods for the definition of baseline coronary flow from published works, as well as three alternative methods to distribute such flow among coronary vessels, in order to assess the impact of these modelling choices on FFR prediction. Finally, we perform a sensitivity analysis where we compare the influence of baseline coronary flow to other parameters that are known to be important, namely, the stenosis geometry and the reduction in coronary peripheral resistance from baseline to hyperemic conditions.

The rest of this paper is structured as follows. In Section 2, we describe the acquisition of patient-specific data (Section 2.1), a reduced-order model for FFR prediction (Section 2.2), the 3D modelling framework used for validation purposes (Section 2.3), the overall modelling strategy for FFR prediction (Section 2.4), several methods to determine baseline coronary flow (Section 2.5) and its distribution among coronary vessels (Section 2.6), and the method by which a sensitivity analysis of predicted FFR to relevant model parameters was performed (Section 2.7). Section 3 provides a summary of main characteristics of patients involved in the study (Section 3.1), results on the validation of the reduced-order model (Section 3.2), and results on the impact of explored modelling strategies on FFR prediction (Section 3.3). Finally, Section 4 includes a detailed analysis of reported results, as well as considerations on the study limitations and the steps to be taken to (a) improve the reduced-order model description to better capture the fluid mechanical aspects of the problem under consideration and (b) reduce uncertainty in FFR predictions.

2 | METHODS

2.1 | Patients and data acquisition

2.1.1 | Recruitment

Patients were recruited as part of an ongoing clinical trial at St. Olavs hospital, Trondheim, Norway.[22] Patients included in this study had undergone CCTA because of chest pain and suspicion of stable CAD. Patients were enrolled with the findings of at least one coronary stenosis at CCTA examination and were further referred to invasive coronary angiography (ICA) with invasive FFR measurements. Exclusion criteria included nondiagnostic quality of the CCTA, previous percutaneous coronary intervention or bypass surgery, contraindications to adenosine, age (75 years or older), obesity (body mass index greater than 40), and hospitalisation due to unstable CAD after CCTA.

2.1.2 | Medical data acquisition

CCTA

CCTA was performed using 2×128 detector row scanners (Siemens dual source Definition Flash) and 256 detector row CT scanners (Revolution CT, GE Healthcare, Waukesha, Wisconsin, US) with a standardised protocol.[23] Left ventricle mass (LVM) was quantified using a commercial software (Syngo.via, Siemens, Germany).

Ultrasound

Echocardiographic imaging was performed using a GE Vivid E95 scanner (GE Vingmed Ultrasound, Horten, Norway). Cardiac output (CO) was calculated on the basis of the cross-sectional area of the left ventricle outflow tract (measured immediately proximal to the points of insertion of the aortic leaflets) and velocity time integral derived from PW Doppler.

Fractional flow reserve

FFR was measured using Verrata Plus (Philips Volcano, San Diego, USA) pressure wires according to standard practice. Intra-coronary nitroglycerine (0.2 mg) was given to all patients before advancing the pressure wire into the coronary arteries, and hyperemia was induced by continuous intravenous infusion of adenosine at a rate of at least 140μg/kg/min. Pressure was measured over several cardiac cycles, and FFR measurements were taken during the nadir (lowest

observed value). After measurement, the interventional cardiologist removed the pressure wire back to the equalisation point at the tip of the guiding catheter to ensure that there was no drift. Invasive pressure tracings were recorded and made available for further processing.

Clinical data

Standard non-invasive diastolic/systolic pressure measurements were performed on both arms as part of clinical routine before ICA using an automatic, digital blood pressure device, Welch Allyn ProBP 3400.

2.2 | Reduced-order model

Here, we briefly describe the methodology presented in Fossan et al[19] for the computation of FFR using a reduced-order model. FFR predictions obtained with the exact setting proposed in Fossan et al[19] will be denoted as FFR_{RO^*}, while predictions obtained using the improved version of the reduced-order model introduced in this section will be denoted as FFR_{RO^*}. This is valid throughout the rest of the paper unless otherwise specified.

2.2.1 | Vessels segmentation and computational domain meshing

Segmentation of coronary vessels is performed using the open-source software ITK-SNAP. [24] The output of ITK-SNAP is a labelled voxel volume identifying segmented vessels and a surface mesh of the segmented volume (in VTK format). Coronary arteries are segmented until their presence is not distinguishable from surrounding tissue. With this, the resulting average (±standard deviation) outlet radius of coronary arteries included in the computational domain is 0.9±0.23 mm. Surface mesh processing, addition of flow extensions, and 3D meshing are performed using the open-source library Vascular Modeling ToolKit (VMTK).[25,26] The 3D volume meshes form the basis for both the reference 3D model and the reduced-order model. For the latter, centerlines are extracted from 3D domains using a centerline extraction algorithm available in VMTK.

2.2.2 | Domain definition

The resulting network of centerlines obtained by the processing steps briefly illustrated in Section 2.2.1 can be conceptually described as a directed graph $G = (V, E)$, where

- V are the vertices of the graph, which in this application can represent junctions/bifurcations, a root node, and terminal nodes of the network, hereafter called outlets.
- E is a set of ordered pairs of vertices, in this case representing vessels.

Graph G will have M edges (or vessels) and N vertices. v_{root} is the vertex at the root of the network, while v^j_{out}, $j = 1, \ ..., N_{out}$, are outlets and v^j_b, $j = 0, \ ..., N_b$, are vertices representing coupling points among vessels, see Figure 1. Vessel e_j is described by a set of K^j nodes produced by the centerline extraction algorithm cited in Section 2.2.1. Each node k^j_l, $l = 1, \ ..., |K^j|$, is marked as belonging to a bifurcation region ($K^j_b \in K^j$), belonging to a stenosis ($K^j_s \in K^j$), or belonging to a 1D domain ($K^j_{1D} \in K^j$). The masking of such regions is explained in detail in Fossan et al.[19]

Here, we modify the domain definition reported in Fossan et al[19] as follows:

- the spacing between nodes k is reduced from 0.5mm to 0.125mm;
- an additional criteria for masking stenotic regions on the basis of the gradient of the radius in the longitudinal direction is added. In Fossan et al,[19] a detected stenosis was marked until the estimated stenosis degree (SD) was below 12%. Here, we require that $SD > 12\% \vee |\frac{dr}{dx}| < 0.05$. In practice, even though the estimated stenosis degree is below 12%, we continue to mark the region as a stenosis if the location represents a compression $\frac{dr}{dx} < 0.05$ or an expansion $\frac{dr}{dx} > 0.05$.

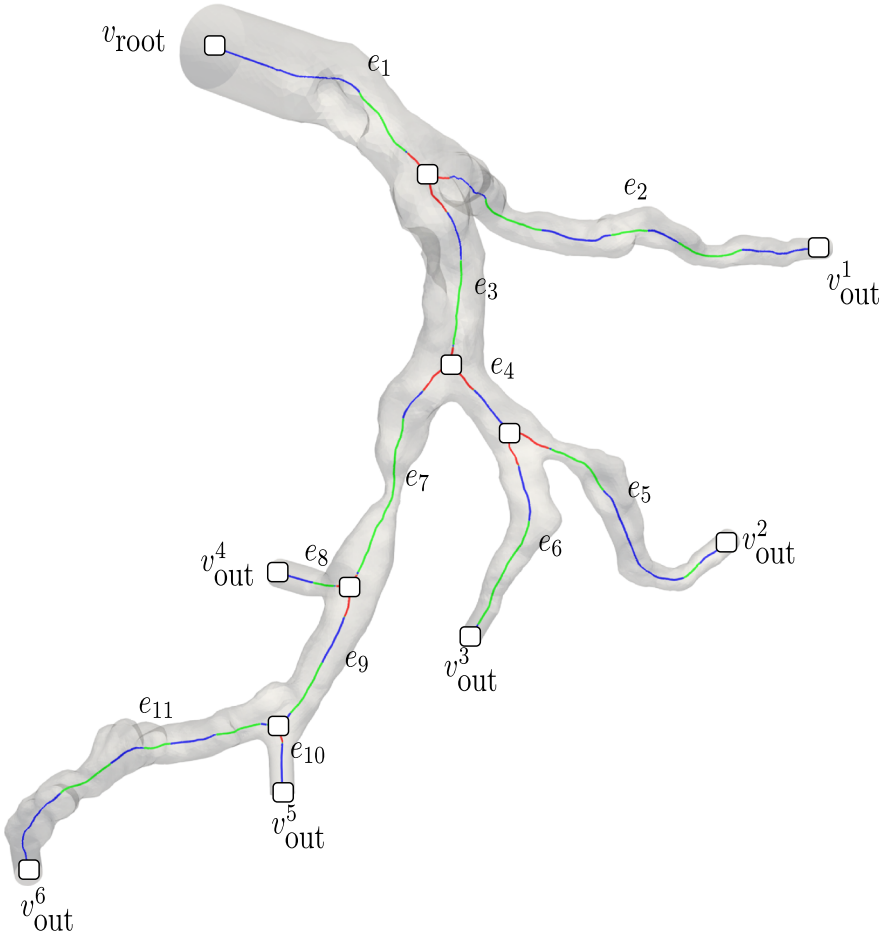

FIGURE 1 Centerline extracted from one subject of the study population. Graph G structure is shown with white rectangles representing vertices. In particular, root, outlet vertices, and edges are evidenced. Edges' regions marked as bifurcation areas are shown in red, stenotic areas are shown in green, and 1D domains are shown in blue. The original 3D segmentation from which centerlines are extracted is shown as a transparent surface

2.2.3 | Mathematical models

Let us consider a single vessel e_j. In regions of e_j labelled as 1D domain, ie, $K^j_{1D} \in K^j$, blood flow is modelled according to a 1D steady state blood flow model, ie,

$$\frac{\partial Q}{\partial x} = 0, \tag{1a}$$

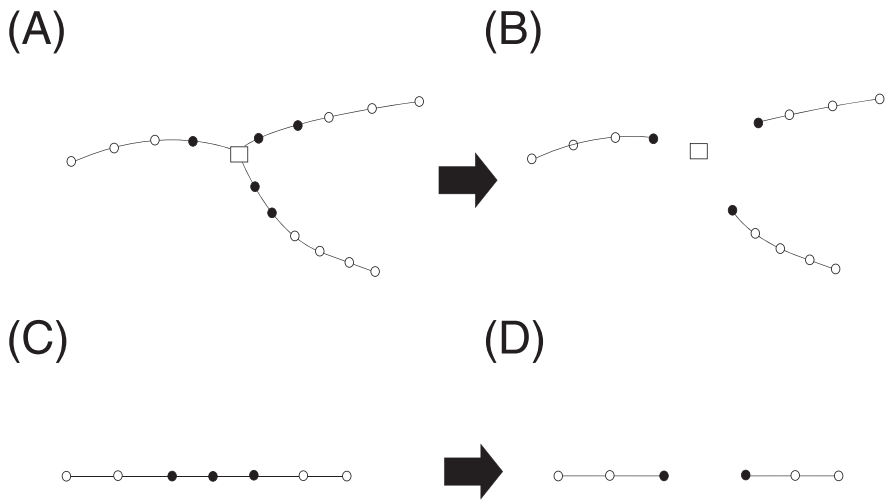

FIGURE 2 A, Vessels at a bifurcation (graph vertex depicted as a hollow square) with corresponding nodes (circles), nodes masked as belonging to the bifurcation region depicted as filled circles. B, Bifurcation region, nodes are collapsed into one node per vessel (filled circles), at which vessels are coupled using (2b). C, Single vessel with corresponding nodes (circles), nodes masked as belonging to a stenotic region are depicted as filled circles. D, Vessel is split into two vessels, stenosis region nodes collapsed into one node per vessel (filled circles), at which the resulting vessels are coupled using (2b) and (3)

$$\frac{\partial}{\partial x}\left(\frac{Q^2}{A}\right) = -\frac{A\partial P}{\rho\,\partial x} + \frac{-2(\zeta+2)\mu\pi Q}{\rho \quad A}, \tag{1b}$$

where A is the cross-sectional area of the vessel, Q is the blood flow rate, and P is the blood pressure. Moreover, ζ=4.31,[19] ρ=1.05g/cm^3 is the blood density, and μ=0.035 dyne/cm^{2}s is the blood viscosity. The cross-sectional area A is assumed constant in time and equal to the area obtained from the segmentation of medical images. Then, the problem unknowns are pressure P and flow rate Q.

Regions masked as bifurcations and stenoses are not modelled using a continuous model. Nodes belonging to such regions are collapsed into a single point, and coupling conditions apply. See Figure 2 for a graphical illustration of this aspect. Coupling for both connection types (bifurcations and stenoses) is performed by enforcing the following relations at the coupling point

$$\sum_{i=1}^{T} Q_i = 0, \tag{2a}$$

$$P_1 + \lambda\frac{\rho}{2}U_1^2 = P_i + \lambda\frac{\rho}{2}U_i^2 + \Delta P_i \quad i = 2,\ \ldots,\ T, \tag{2b}$$

where T is the number of vessels sharing a vertex with the bifurcation/stenosis. For stenoses, we have that T=2, while in the case of bifurcations, we have $T \geq 2$. ΔP is an additional pressure loss, and λ is a coefficient that can assume values between zero and one. At bifurcations, ΔP is set to zero and λ is set to one, so that Equation (2a) describes continuity of total pressure. At coupling points representing stenoses, we set λ=0, and ΔP is computed as proposed in Seeley and Young,[27] namely

$$\Delta P = \frac{K_v\mu}{A_0 D_0}Q + \frac{K_t\rho}{2A_0^2}\left(\frac{A_0}{A_s}-1\right)^2 Q|Q|, \tag{3}$$

where A_0 and A_s refer to cross-sectional areas of the normal and stenotic segments, respectively. Similarly, D_0 and D_s represent the normal and stenotic diameters. Furthermore, K_v and K_t are empirical coefficients, with $K_v = 32(0.83L_s + 1.64D_s)\cdot(A_0/A_s)^2/D_0$, K_t=1.52,[27] whereas L_s is the length of the stenosis.

2.2.4 | Boundary conditions

In this work, we consider two alternative sets of outlet boundary conditions: prescribed flow rate at outlets or resistive elements coupled to outlets. See Section 2.4 for motivation on the two different setups introduced here.

Prescribed flow rates at outlets

Pressure is prescribed at v_{root}, namely $P_{\text{root}} = \hat{P}_{\text{root}}$, where $\hat{P}_{\text{root}}$ is the prescribed pressure. Then, we set $Q^j_{\text{out}} = \hat{Q}^j$, $j = 1,\ \ldots,\ N_{\text{out}}$, where $\hat{Q}^j$, $j = 1,\ \ldots,\ N_{\text{out}}$, are the flows to be prescribed deriving from methods described in Sections 2.5 and 2.6. Defining flow rate at outlets implies that flow rate over the entire network is fixed. Then, the only remaining unknown is pressure along 1D domains, and pressure drops over stenotic regions. Such pressure is obtained integrating (1) for Q given along the 1D domains and evaluating coupling relations (2b) and (3) where appropriate. A reasonable strategy is to start at v_{root} and traverse the entire tree, but other choices are possible.

Resistive elements coupled to outlets

As in the previous case, pressure is prescribed at v_{root}, namely $P_{\text{root}} = \hat{P}_{\text{root}}$. Then, we consider resistive elements coupled to outlets with resistances R^j_{out}, $j = 1,\ \ldots,\ N_{\text{out}}$. In this case, flow rate is unknown over the entire network, and a nonlinear algebraic system has to be solved to find the flow rates at outlets Q^j_{out}, $j = 1,\ \ldots,\ N_{\text{out}}$, which solve (1), (2b), (3), and $P_{\text{root}} - \hat{P}_{\text{root}} = 0$. More details on the numerical treatment of the modelling setup strategies presented here are given in Fossan et al.[19]

2.3 | 3D modelling

3D simulations are used to validate the reduced-order model proposed in Fossan et al[19] and improved in this work. These simulations are performed considering segmented coronary trees as rigid domains with a prescribed pressure as inlet boundary condition and either prescribed flows (via prescribed parabolic velocity profile) or lumped-parameter models attached to each network outlet, according to the modelling pipeline described in Section 2.4. Furthermore, the flow is assumed laminar, and blood is modelled as an incompressible Newtonian fluid. The open-source library CBCFLOW,[28] based on FEniCS[29] is used to solve the resulting mathematical model. The incompressible Navier-Stokes equations are solved using the incremental pressure correction scheme, described in Simo and Armero.[30] Tetrahedral elements compose the computational mesh where the velocity field is approximated using piecewise-quadratic polynomials, while linear polynomials are used for pressure. The solver implementation follows very closely the one reported in Mortensen and Valen-Sendstad.[31] 3D meshes were constructed using the open-source library VMTK.[25,26] The meshing refinement level was determined by a meshing algorithm parameter called edge-length factor l_f, which was set to l_f=0.21 for all simulations. A mesh independence study showed that such discretisation provides mesh-independent FFR predictions for a set of four patient-specific geometries. A full description of the underlying mathematical models and their numerical treatment is provided in Fossan et al[19] and references cited therein.

2.4 | Overall modelling strategy

FFR is normally measured at one or more points in the coronary tree. In the current computational context, we simulate a hyperemic state for the entire coronary tree. Therefore, we refer to a hyperemic state as the condition under which virtual FFR measurements are performed. Assuming that a network of coronary branches for a given patient with related parameters is available (see Section 2.2), we proceed as follows in order to obtain a hyperemic state:

1. define total baseline coronary flow by one of the methods described in Section 2.5: q;
2. distribute flows among the network's N_{out} outlets according to one of the methods described in Section 2.6: $Q_{\text{out},l}$, with l=1,...,N_{out};
3. perform a simulation with prescribed inlet pressure P_{root}=P_{proximal} and prescribed outlet flows defined in previous step to find $P^{\text{bln}}_{\text{out},l}$, with $l = 1, \ ..., N_{\text{out}}$;
4. compute resistances at outlets as
$$R^{\text{bln}}_{\text{out},l} = \frac{P^{\text{bln}}_{\text{out},l} - P_v}{Q^{\text{bln}}_{\text{out},l}}, \text{ with } l = 1, \ ..., N_{\text{out}}, \tag{4}$$
where $P^{\text{bln}}_{\text{out},l}$ is the pressure at the l-th outlet resulting from the simulation performed in previous step and P_v is a reference venous pressure, which is set to P_v=5 mmHg throughout this work;
5. perform a simulation with prescribed inlet pressure P_{root}=P_{proximal} and prescribed resistances at outlets. Such resistances are computed as
$$R^{\text{hyp}}_{\text{out},l} = \frac{R^{\text{bln}}_{\text{out},l}}{\text{TCRI}}, \text{ with } \ l = 1, \ ..., N_{\text{out}}, \tag{5}$$
where TCRI is the so-called total coronary resistance index, ie, the factor by which peripheral coronary resistance drops from its value at baseline conditions to its value in hyperemia. In this work we use TCRI=4, unless otherwise stated.[4]

TABLE 1 Parameters needed to run a simulation using pipeline described in Section 2.4

Parameter/Data	Symbol	Source/Equation/Table
Coronary tree centerlines with radii	-	post-processed CCTA-derived segmentation
Pressure at inlet	P_{proximal}	Clinical non-invasive measurement
Baseline flow	q	Table 3
Branch split	-	Table 4 or coupled branches (see Section 2.6)
Total coronary resistance index	TCRI	TCRI=4, as in Wilson et al[4]

[a]Abbreviation: CCTA, coronary computed tomography angiography.

Simulation results from point 5 of the previous list represent the hyperemic state from which FFR can be evaluated at any point of the network as

$$\mathrm{FFR}^{j}_{\mathrm{RO}} = \frac{P_j}{P_{\mathrm{proximal}}}, \tag{6}$$

where P_j is the predicted pressure at the jth node of the network. We remind the reader about the fact that if predictions are obtained with the setting proposed in Fossan et al,[19] ie, without the modifications introduced in Section 2.2.2, then those predictions will be denoted as $\mathrm{FFR}_{\mathrm{RO}^*}$. Table 1 summarises necessary data and parameters for prediction of FFR with the reduced order model.

2.5 | Methods for baseline coronary flow estimation

In this work, we explore a number of methods to estimate baseline coronary flow, q. In selecting the methods to be used, we sought to include methods that use different types of data. In particular, we included methods that rely on CO estimation, as well as methods that use LVM and a method based on population studies. A description of such methods follows.

2.5.1 | CO-based methods for baseline coronary flow estimation

We consider two alternative methods to determine CO. The first method consists of simply using the CO derived from patient-specific ultrasound (US) measurements acquired as explained in Section 2.1.2. CO derived from US measurements will be called $\mathrm{CO}_{\mathrm{US}}$ hereafter. The second method uses a formula to estimate stroke volume from patient-specific parameters.[32] Such formula, originally proposed in de Simone et al,[33] is given as

$$\mathrm{SV} = \mathrm{PP}^{*} \times [(0.013 \times \mathrm{W}) - (0.007 \times \mathrm{Y}) - (0.004 \times \mathrm{HR}) + 1.307], \tag{7}$$

where W is weight in kilograms, Y is age in years, and HR is heart rate in beats per minute. Moreover, PP^{*} is

$$\mathrm{PP}^{*} = (0.49 \times \mathrm{PP}) + (0.3 \times \mathrm{Y}) + 7.11, \tag{8}$$

where PP is pulse pressure, PP=SBP−DBP, with SBP and DBP being systolic and diastolic blood pressure (in mmHg), respectively. Then, CO is computed as

$$\mathrm{CO}_{\mathrm{DeSimone}} = \mathrm{HR} \times \mathrm{SV}. \tag{9}$$

Once CO is estimated by either of the two methods, we compute baseline coronary flow as

$$q^{\mathrm{X}}_{\mathrm{Guyton}} = \gamma\, \mathrm{CO}_{\mathrm{X}}, \tag{10}$$

where γ=0.045 is the fraction of CO that flows into the coronary branches,[34] and X={US,DeSimone} are the two considered CO estimation methods.

2.5.2 | LVM-based methods for baseline coronary flow estimation

Alternatively to the use of CO to determine total baseline coronary flow q, several investigators have used LVM to perform such estimate. Here, we select two methods and propose modifications to them. In Kishi et al,[35] q is computed as

$$q_{\mathrm{Kishi}} = \beta \times \mathrm{TMM}, \tag{11}$$

where β=0.8 mL/min/g is a reference value for myocardial tissue perfusion,[36] and TMM stands for total myocardial mass, computed as

TABLE 2 Baseline coronary flows from Sakamoto et al[40]

Branch	Symbol	Flow, mL/min (Right-dominant)	Flow, mL/min (Left-dominant)
Left branch	$q_{\text{Sakamoto}}^{\text{LB}}$	156.58	209.27
Right branch	$q\text{Sakamoto}^{\text{RB}}$	113.42	57.73
Total	q_{Sakamoto}	270.00	267.00

$$\text{TMM} = \frac{3}{2} \times \text{LVM}. \tag{12}$$

It is worth noting that no other patient-specific information than LVM is used. A method that accounts for additional patient-specific information is the one used for FFR prediction in Sharma et al.[37] In this case, the observed association between the product SBP×HR is considered in the computation of baseline flow, which reads

$$q_{\text{Sharma}} = (0.08 \times (0.7 \times \text{HR} \times \text{SBP} \times 0.001 - 0.4)) \times \text{TMM}, \tag{13}$$

where TMM is computed with (12). Since, as it will be shown later in Section 3.1, Table 2, baseline coronary flows computed using (11) and (13) are very low compared with reference values, we propose to modify both methods. The reason for the underestimation of baseline coronary flow in these cases is related to the rather low TMM derived from the hypothesis stated in (12). In both modified methods, we use

$$\text{TMM}_{\text{Molina}} = 2.4 \times LVM. \tag{14}$$

The constant value 2.4 was determined by considering that the ratio of reference TMM reported in Molina and DiMaio[38,39] over LVM for patients included in this study (2.39 (0.34) and 2.34 (0.42) for men and women, respectively). Moreover, in the case of q_{Sharma}, the constant 0.08 was replaced by 0.14 in order to force average flow over the population to be in accordance with reference values.[40] See Table 2 for details. Modified baseline flow estimates are denoted as $\widehat{q}_{\text{Kishi}}$ and $\widehat{q}_{\text{Sharma}}$ for q_{Kishi} and q_{Sharma}, respectively.

2.5.3 | Population-based methods for baseline flow estimation

Here, we simply specify flows to left and right coronary branches as specified in Sakamoto et al. [40] Average flows are differentiated according to the dominance of the coronary vasculature. Table 2 summarises the different values for total coronary flow, as well as for left and right branches.

Table 3 summarises the different methods used to determine coronary flow and how they are computed.

TABLE 3 Summary of baseline coronary flow estimation methods

Method	Data	Equations
$q_{\text{Guyton}}^{\text{US}}$	CO_{US}	(10)
$q_{\text{Guyton}}^{\text{DeSimone}}$	W, Y, HR, SBP, DBP	(10)
q_{Kishi}	LVM	(11), (12)
$\hat{q}_{\text{Kishi}}$	LVM	(11), (14)
q_{Sharma}	LVM, HR, SBP	(13), (12)
$\hat{q}_{\text{Sharma}}$	LVM, HR, SBP	(13)-mod, (14)
q_{Sakamoto}	Table 2	-

Note. All data used was acquired non-invasively in ambulatory conditions unless otherwise stated.

Abbreviation: CO, cardiac output; DBP, diastolic blood pressure; HR, heart rate; LVM, left ventricle mass; SBP, systolic blood pressure; US, ultrasound; W, weight (in kilograms); Y, age (in years).

2.6 | Flow distribution

There is a variety of methods used in the literature to distribute baseline coronary flow among the coronary vessels. A major difference is given by the fact that some practitioners model a single branch (left or right), while others consider both branches simultaneously. In order to account for this aspect, we have applied the methods described below in two different settings, namely, applying the methods on single branches or on both coupled branches.

2.6.1 | Distal Murray

Murray's law[41] is the most commonly used method to distribute coronary flow; see previous studies[37,42] for example. It expresses a proportionality between flow and vessel diameter

$$Q \propto d^{\xi}, \tag{15}$$

with ξ=3 from theoretical considerations on minimum work. Distal Murray (DM) flow distribution implies that for a given network with N_{out} outlets, flow is distributed among all outlets using (15) and outlets' diameters.

2.6.2 | Proximal Murray

In this case, one traverses a given network from its root, and flow is split at each bifurcation applying (15) among daughter vessels. The diameter used here was taken as the average vessel diameter, computed over vessel nodes that were not marked as belonging to stenoses or bifurcation areas. See Section 2.2 for an explanation and further references on how these nodes are marked. This method was used in previous studies,[35,43] in the context of FFR prediction.

2.6.3 | Transluminal Attenuation Gradient

Here, we implement the method proposed in Kishi et al,[35] where authors hypothesise an inverse relation between flow and transluminal attenuation gradient (TAG), ie, $Q \propto -1/\text{TAG}$. The interesting feature of this approach is that it uses information on flow distribution properties of a given patient by directly looking into how contrast is advected in the coronary tree during CCTA acquisition. TAG is essentially the gradient of voxel intensities, quantified as Hounsfield Units (HU) in the CCTA image averaged along a given vessel. TAG is computed for each terminal point of the vessel network by computing HU along centerline nodes and fitting a first-order polynomial to the resulting data points (arc-length versus HU: $\text{HU}(x)=\text{HU}_0+\text{TAG}\cdot x$, with x the centerline arc-length). Intensities along the path are computed by averaging CCTA voxel intensities around each centerline node. Candidate voxels are those in a volume of 5×5×5 voxels centred at a given centerline node. In order to be included, a candidate voxel has to fall within the segmented vessel lumen and has to have a HU value that is below a threshold in order to exclude calcifications and artefacts. Such threshold is set equal to the average plus two standard deviations of HU values for all voxels contained in the segmented lumen volume. For a detailed definition of TAG and its computation in coronary trees; see Kishi et al[35] and references cited therein. TAG is computed for each patient considered in this study using CCTA images, segmented vessels lumen volume, and extracted centerlines.

2.6.4 | Branch flow split for single branch distribution

In the case in which a single coronary branch is considered for simulation, a further assumption is necessary since we depart from total baseline coronary flow, and a branch-specific flow is needed. Two strategies are followed. One strategy consists of splitting flow between left and right branches as observed in Sakamoto et al[40] and reported in Table 4. The second one regards simply imposing average coronary flows to left and right branches, specified in Table 2.

TABLE 4 Baseline coronary flow splits derived from Sakamoto et al[40]

Branch	Right-Dominant Percentage of Total Flow	Left-Dominant Percentage of Total Flow
Left branch	58.00	78.38
Right branch	42.00	21.62

TABLE 5 Summary of baseline coronary flow estimation and split methods

Branch Treatment	Baseline Flow	Branch Split	Flow Distribution
Single branch	$q^{\mathrm{US}}_{\mathrm{Guyton}}$	Table 4	DM/PM/TAG
	$q^{\mathrm{DeSimone}}_{\mathrm{Guyton}}$	Table 4	DM/PM/TAG
	$\bar{q}^{\mathrm{US}}_{\mathrm{Guyton}}$	Table 4	DM/PM/TAG
	q_{Kishi}	Table 4	DM/PM/TAG
	$\hat{q}_{\mathrm{Kishi}}$	Table 4	DM/PM/TAG
	q_{Sharma}	Table 4	DM/PM/TAG
	$\hat{q}_{\mathrm{Sharma}}$	Table 4	DM/PM/TAG
	q_{Sakamoto}	Table 2, first and second rows	DM/PM/TAG
Coupled branches	$q^{\mathrm{US}}_{\mathrm{Guyton}}$	-	DM/PM/TAG
	$q^{\mathrm{DeSimone}}_{\mathrm{Guyton}}$	-	DM/PM/TAG
	$\bar{q}^{\mathrm{US}}_{\mathrm{Guyton}}$	-	DM/PM/TAG
	q_{Kishi}	-	DM/PM/TAG
	$\hat{q}_{\mathrm{Kishi}}$	-	DM/PM/TAG
	q_{Sharma}	-	DM/PM/TAG
	$\hat{q}_{\mathrm{Sharma}}$	-	DM/PM/TAG
	q_{Sakamoto}	Table 2, third row	DM/PM/TAG

Abbreviation: DM, distal Murray; PM, proximal Murray; TAG, transluminal attenuation gradient.

Having defined the three flow distribution strategies that will be explored in this work, we can define a set of simulation settings that will be used for each of the baseline flow estimation methods described in Section 2.5 and summarised in Table 3. In fact, for each one of those baseline flows, we have Y_{Z} flow splits, with Y={PM,DM,TAG} and Z={S,C}. S and C correspond to cases where flow distribution is applied to single and coupled branches, respectively. Table 5, together with Table 3, provides the reader with a complete overview of all modelling assumption combinations used in this study, so that the equations and parameters used for a specific simulation setup can be easily retrieved.

2.7 | Sensitivity analysis

We conduct uncertainty quantification and sensitivity analysis (UQ&SA) to rank the influence of uncertain input parameters on FFR prediction. In Fossan et al,[19] a wide range of parameters were analysed in terms of UQ&SA; however, the most influential parameters were those related to coronary flow, TCRI, and minimum stenotic radius. Other input parameters such as P_{proximal}, Murray coefficient, and rheological parameters (ρ, μ) were less influential. On the basis of these considerations, we perform a sensitivity analysis on the uncertain input parameters q, TCRI, and SD, with the uncertainty in SD affecting the minimum radius. q was modelled as a (truncated at ± 3 std) normal distribution with a mean and standard deviation deriving from the per patient mean and standard deviation obtained with four of the patient-specific baseline coronary flow estimates studied in this work, $q^{\mathrm{US}}_{\mathrm{Guyton}}$, $q^{\mathrm{DeSimone}}_{\mathrm{Guyton}}$, $\hat{q}_{\mathrm{Kishi}}$, and $\hat{q}_{\mathrm{Sharma}}$. We model the hyperemic factor TCRI as a gamma distribution with shape parameter 3, scale factor 0.75, and shifted to 1.[19] For our dataset of 105 FFR measurements, clinically relevant stenoses were quantified in terms of SD using QCA and $\mathrm{QCA_{CT}}$, where $\mathrm{QCA_{CT}}$ denotes QCA evaluated on the basis of segmented geometries. The standard deviation of $\mathrm{QCA}-\mathrm{QCA_{CT}}$ was 20% SD. To account for the uncertainty in stenosis geometry, we introduce a global parameter ΔSD, to be applied to all stenotic regions of a network such that the stenosis degree is given by $\mathrm{SD}=\mathrm{SD}_{\mathrm{segmented}}+\Delta\mathrm{SD}$, where $\mathrm{SD}_{\mathrm{segmented}}$ is the stenosis degree obtained from the original segmentation. Since we adopt a conservative approach where all detected stenoses are included in a global parameter, we model ΔSD as a normal distribution with a mean of 0 and with a standard deviation of 15%.

Sobol sensitivity indices, first-order (S_i) and total ($S_{T,i}$), are widely employed[44] and defined as

$$S_i = \frac{\mathbb{V}[\mathbb{E}[Y \quad |Z_i]]}{\mathbb{V}[Y]}, \tag{16a}$$

$$S_{T,i} = 1 - \frac{\mathbb{V}[\mathbb{E}[Y|\mathbf{Z}_{\neg i}]]}{\mathbb{V}[Y]}. \tag{16b}$$

Here, $\mathbb{E}[Y|\mathbf{Z}_{\neg i}]$ represents the expected value of the output Y for a fixed value of the uncertain input, Z_i, and $\mathbb{V}[X]$ is the variance of some variable, X. $\mathbf{Z}$ is a vector that represents the uncertain input variables, ($\mathbf{Z} = [q, \text{TCRI}, \text{SD}]$), and $\mathbf{Z}_{\neg i}$ contains all elements of $\mathbf{Z}$ except Z_i. SA results (which are obtained on a per patient basis) are summarised by averaging the first-order and total Sobol sensitivity indices over the population. Moreover, we compute weighted first-order sensitivity indices

$$AS_i = \frac{\sum_{k=1}^{n} S_i^k \mathbb{V}[Y_k]}{\sum_{k=1}^{n} \mathbb{V}[Y_k]}, \tag{17}$$

and total sensitivity indices

TABLE 6 Study population characteristics. If not specified, presented results are reported as "mean (standard deviation)"

Characteristic	Units	Mean(std)
Generic data		
No. of patients	-	63
No. of male patients	Datum (percentage)	35 (55.56)
Age	y	59.87 (7.77)
Height	cm	173.62 (10.03)
Weight	kg	85.28 (15.02)
Body mass index	kg/cm^2	28.17 (3.69)
MAP	mmHg	103.48 (10.70)
Cardiac output	L per min	5.07 (0.97)
CAD risk factor	Datum (percentage)	
Diabetes		8 (12.70)
Hypertension		33 (52.38)
Dislipidemia		18 (28.57)
Smoking		11 (17.46)
Previous CAD events		0 (0)
Invasive FFR measurements		
FFR	-	0.81 (0.14)
FFR per vessel prevalence	Datum (percentage)	33/105 (31.43)
FFR per patient prevalence	Datum (percentage)	25/63 (39.68)
Lesions location		
LAD artery	Datum (percentage)	45 (42.86)
RCA	Datum (percentage)	22 (20.95)
LCX artery	Datum (percentage)	13 (12.38)
Diagonals	Datum (percentage)	12 (11.43)
Marginals	Datum (percentage)	8 (7.62)
RPDA	Datum (percentage)	4 (3.81)

[a]Abbreviation: CAD, coronary artery disease; FFR, fractional flow reserve; LAD, left anterior descending; LCX, left circumflex; MAP, mean arterial pressure; RCA, right coronary artery; RPDA, right posterior descending artery.

TABLE 7 LVM and TMM quantification from CCTA. Reported values are average (standard deviation)

Sex	LVM, g	Reference LVM, g[48]	TMM (12)	TMM (14)	Reference TMM[38,39]
Male	141 (21)	116 (20)	211 (32)	338 (51)	331 (56)
Female	108 (19)	85 (14)	162 (28)	259 (45)	245 (52)

[a]Abbreviation: CCTA, coronary computed tomography angiography; LVM, left ventricle mass; TMM, total myocardial mass.

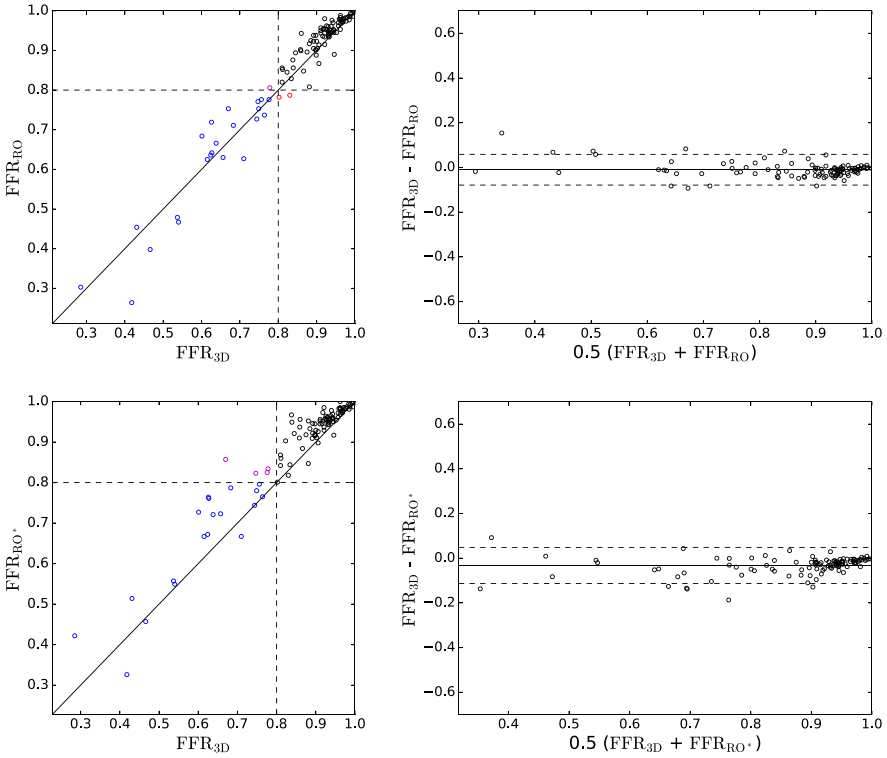

FIGURE 3 Scatter plot and Bland-Altman of FFR_{RO} vs FFR_{3D} (top row) and FFR_{RO^*} vs FFR_{3D} (bottom row). The rest of the settings are single branch treatment, q^{US}_{Guyton} baseline flow, and DM flow distribution. DM, distal Murray; FFR, fractional flow reserve; RO, reduced-order; US, ultrasound

$$AS_{T,i} = \frac{\sum_{k=1}^{n} S^k_{T,i} \mathbb{V}[Y_k]}{\sum_{k=1}^{n} \mathbb{V}[Y_k]}, \tag{18}$$

where Si^k and $S^k_{T,i}$ are the sensitivities due to input i for FFR-prediction k, and $\mathbb{V}[Y_k]$ is the variance of FFR-prediction k.[19,45]

Measures of uncertainty and sensitivity are estimated by the Monte Carlo method as described by Saltelli,[46] and the accuracy of UQ&SA results are assessed by evaluating the standard deviation of the estimates from 10 bootstrapped samples[47] until the standard deviation is below 0.033 (ie, 99% confident that obtained value is within ±0.1.).

TABLE 8 Comparison of FFR_{RO} vs FFR_{3D} and FFR_{RO^*} vs FFR_{3D} for selected 1D settings. Settings are single branch treatment, q^{US}_{Guyton} baseline flow, and DM flow distribution

Terminal	RO Model Version	*a*	*b*	*r*	$FFR_X - FFR_{3D}$	Acc.	Sen.	Spe.	PPV	NPV
Resistive	X=RO	1.06	−0.04	0.98	−0.01 (0.03)	97.14	95.65	97.56	91.67	98.77
	X=RO*	0.89	0.12	0.96	−0.03 (0.04)	96.19	82.61	100	100	95.35
3D flows	X=RO	1.05	−0.03	0.94	−0.013 (0.056)	96.19	95.65	96.34	88.00	98.75
	X=RO*	0.77	0.24	0.90	−0.043 (0.061)	92.38	65.22	100.00	100.00	91.11

Note. *a* and *b* are coefficients for linear fitting: $FFR_X = a\,FFR_{3D} + b$, while *r* is Pearson correlation coefficient.

Abbreviation: DM, distal Murray; FFR, fractional flow reserve; RO, reduced-order; US, ultrasound.

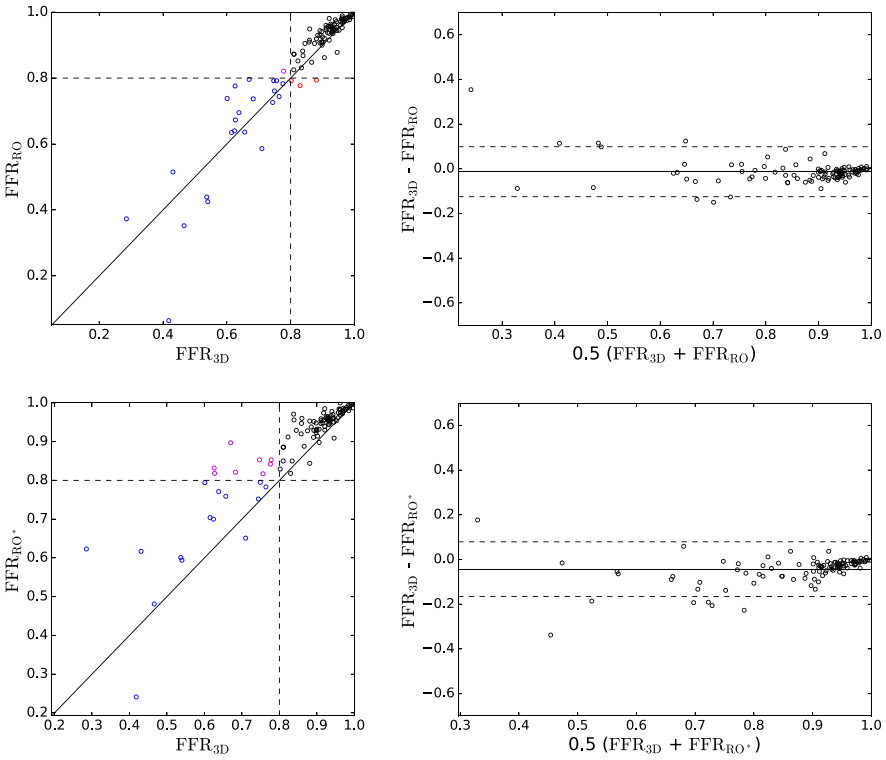

FIGURE 4 Scatter plot and Bland-Altman of FFR_{RO} vs FFR_{3D} (top row) and FFR_{RO^*} vs FFR_{3D} (bottom row). The rest of the settings are single branch treatment, q^{US}_{Guyton} baseline flow, and DM flow distribution. FFR_{RO} and FFR_{RO^*} were obtained by prescribing the hyperemic outlet flows from the 3D solution instead of running the FFR-pipeline described in Section 2.4. DM, distal Murray; FFR, fractional flow reserve; RO, reduced-order; US, ultrasound

3 | RESULTS

3.1 | Patient population and invasive measurements characteristics

A total of 63 patients that underwent invasive angiography and FFR measurements after clinical and CCTA examinations indicated stable CAD were recruited. From these patients, a total of 105 FFR measurements were collected. FFR measurements had a mean of 0.81 and a standard deviation of 0.14, with a per vessel positive FFR prevalence of 31.43% and a per patient positive FFR prevalence of 39.68% for a cut-off value of $FFR \leq 0.8$. See Table 6 for a summary of population characteristics.

Table 7 shows a comparison of LVM for the study population versus reference values taken from a large CT study for healthy young subjects.[48]

TABLE 9 Comparison of FFR_A vs FFR_B for selected cases where FFR_{3D} was available. Other settings common to all simulations are single branch treatment and q^{US}_{Guyton} baseline flow

Comparison Type	Flow Distribution	*a*	*b*	*r*	$FFR_A - FFR_B$	Acc.	Sen.	Spe.	PPV	NPV
RO vs 3D	DM	1.06	−0.04	0.98	−0.01 (0.03)	97.14	95.65	97.56	91.67	98.77
	PM	1.06	−0.04	0.98	−0.01 (0.03)	95.24	84.62	98.73	95.65	95.12
	TAG	1.08	−0.05	0.98	−0.01 (0.04)	94.29	80.00	100.00	100.00	92.59
RO vs invasive measurement	DM	0.64	0.34	0.58	−0.05 (0.13)	81.90	57.58	93.06	79.17	82.72
	PM	0.63	0.34	0.57	−0.04 (0.14)	80.95	54.55	93.06	78.26	81.71
	TAG	0.77	0.21	0.62	−0.03 (0.14)	83.81	60.61	94.44	83.33	83.95
3D vs invasive measurement	DM	0.62	0.35	0.60	−0.04 (0.12)	80.95	54.55	93.06	78.26	81.71
	PM	0.64	0.33	0.62	−0.03 (0.12)	81.90	60.61	91.67	76.92	83.54
	TAG	0.75	0.22	0.66	−0.01 (0.12)	83.81	69.70	90.28	76.67	86.67

Note. *a* and *b* are coefficients for linear fitting: $FFR_A = a\,FFR_B + b$, while *r* is Pearson correlation coefficient.

Abbreviation: DM, distal Murray; FFR, fractional flow reserve; PM, proximal Murray; RO, reduced-order; TAG, transluminal attenuation gradient; US, ultrasound.

TABLE 10 Comparison of total baseline coronary flow, q, and coronary perfusion assuming TMM is 1.5 or 2.4 times LVM

	$q^{\text{US}}_{\text{Guyton}}$	$q^{\text{DeSimone}}_{\text{Guyton}}$	$\bar{q}^{\text{US}}_{\text{Guyton}}$	q_{Sakamoto}	q_{Kishi}	$\hat{q}_{\text{Kishi}}$	q_{Sharma}	$\hat{q}_{\text{Sharma}}$
q, mL/min	227±42	278±53	229±0	270±1	151±32	241±52	93±27	261±77
q/(1.5×LVM), mL/g/min	1.2±0.3	1.5±0.5	1.3±0.3	1.5±0.3	0.8±0.0	1.3±0.0	0.5±0.1	1.4±0.3
q/(2.4×LVM), mL/g/min	0.8±0.2	1.0±0.3	0.8±0.2	0.9±0.2	0.5±0.0	0.8±0.0	0.3±0.1	0.9±0.2

Note. Reported values are averages (standard deviation) for all 63 patients.

Abbreviation: LVM, left ventricle mass; TMM, total myocardial mass.

3.2 | Validation of reduced-order model versus 3D

Figure 3 shows scatter plots and Bland-Altman plots for a comparison of FFR predicted by 3D and reduced-order models, while a numerical characterisation of the comparison is given in Table 8. The modelling setup used to obtain such results was described in Section 2.4, while the particular model parameter definition used included single branch treatment, $q^{\text{US}}_{\text{Guyton}}$ baseline coronary flow, and DM flow distribution. Results are shown for the domain definition setup described in Fossan et al[19] and the modified version proposed here. Figure 4 and Table 8 show results for FFR predictions obtained with current method and the one originally proposed in Fossan et al[19] for the case in which the hyperemic simulation is performed replacing resistive elements at outlets with the flows extracted from 3D simulations.

Table 9 reports indexes on the agreement of predicted FFR by the reduced-order model with respect to results obtained using 3D simulations, as well as comparisons of reduced-order model predicted FFR and 3D model predicted FFR versus invasive measurements, for the three flow distribution strategies considered in this work.

3.3 | Baseline coronary flow and FFR prediction by different strategies

Table 10 shows resulting baseline coronary flows and perfusion indexes for strategies proposed in Section 2.5.

Table 11 shows accuracy indexes for predicted FFR with respect to invasive FFR for all possible combinations of baseline flow estimation and flow distribution strategies. Only results using q_{Kishi} and q_{Sharma} are not reported, since baseline flows obtained with these two methods resulted in values well below physiological ranges with 151±32mL/min and 93±27mL/min for q_{Kishi} and q_{Sharma}, respectively (see Table 10). Moreover, Table 12 shows results for coupled branches treatment and $\bar{q}^{\text{US}}_{\text{Guyton}}$ baseline flow on a per vessel basis, differentiating results among (major branches departing from) left anterior descending artery (LAD), left circumflex artery (LCX), and right coronary artery (RCA).

3.4 | UQ and SA

Figure 5 shows results from the sensitivity analysis described in Section 2.7 in terms of the averaged and uncertainty weighted (see (17) and (18)) sensitivity indices. In the top panel, we have summarised the sensitivity indices when all 105 cases are considered, whereas in the bottom panel, only cases (N=37) where average predicted FFR is $0.7<FFR_{\text{RO}}<0.9$ are considered.

4 | DISCUSSION

4.1 | Patient population and derived measurements

The study population is considered representative for patients with suspected CAD being referred for CCTA.

Since two of the methods to determine baseline coronary flow introduced in Section 2.5 depend on TMM, it is important to discuss results presented in Table 7. We observe that average LVM values for males and females are normally larger than the ones reported as reference values for healthy subjects in Fuchs et al.[48] The higher-than-reference LVM values observed for the population under study are supported by reported left ventricle hypertrophy in patients with stable treated chest angina[49] and by the fact that elevated LVM is a recognised marker for cardiovascular risk.[50] Moreover, TMM values obtained using relation (12) are well below reference values, while usage of relation (14) produces TMM estimates slightly above TMM reference values, in line with what is observed for LVM values. This apparent underestimation of TMM by relation (12) will have an impact in flow computations, as we will discuss later in Section 4.3.

TABLE 11 Comparison of FFR_{RO} vs FFR_m for all cases with exception of those obtained using q_{Kishi} and q_{Sharma}; see text for motivation

Branch Treatment	Baseline Flow	Flow Distribution	*a*	*b*	*r*	$FFR_{RO}-FFR_m$	Acc.	Sen.	Spe.	PPV	NPV
Single	q^{US}_{Guyton}	DM	0.64	0.34	0.58	−0.05 (0.13)	81.90	57.58	93.06	79.17	82.72
		PM	0.63	0.34	0.57	−0.04 (0.14)	80.95	54.55	93.06	78.26	81.71
		TAG	0.77	0.21	0.62	−0.03 (0.14)	83.81	60.61	94.44	83.33	83.95
	$q^{DeSimone}_{Guyton}$	DM	0.72	0.25	0.57	−0.02 (0.15)	81.90	63.64	90.28	75.00	84.42
		PM	0.71	0.25	0.57	−0.02 (0.15)	79.05	57.58	88.89	70.37	82.05
		TAG	0.87	0.11	0.61	0.00 (0.15)	82.86	69.70	88.89	74.19	86.49
	$\bar{q}^{US}_{Guyton}$	DM	0.66	0.32	0.57	−0.05 (0.14)	81.90	57.58	93.06	79.17	82.72
		PM	0.65	0.33	0.56	−0.04 (0.14)	80.95	57.58	91.67	76.00	82.50
		TAG	0.79	0.19	0.61	−0.02 (0.14)	86.67	69.70	94.44	85.19	87.18
	$q_{Sakamoto}$	DM	0.75	0.23	0.58	−0.03 (0.15)	84.76	69.70	91.67	79.31	86.84
		PM	0.73	0.24	0.58	−0.02 (0.15)	82.86	69.70	88.89	74.19	86.49
		TAG	0.88	0.10	0.62	0.00 (0.15)	84.76	72.73	90.28	77.42	87.84
	$\hat{q}_{Kishi}$	DM	0.64	0.33	0.57	−0.04 (0.14)	83.81	63.64	93.06	80.77	84.81
		PM	0.63	0.34	0.55	−0.04 (0.14)	83.81	63.64	93.06	80.77	84.81
		TAG	0.77	0.20	0.60	−0.02 (0.14)	85.71	66.67	94.44	84.62	86.08
	$\hat{q}_{Sharma}$	DM	0.67	0.31	0.56	−0.04 (0.14)	81.90	60.61	91.67	76.92	83.54
		PM	0.65	0.32	0.56	−0.03 (0.14)	82.86	60.61	93.06	80.00	83.75
		TAG	0.80	0.17	0.60	−0.01 (0.15)	83.81	60.61	94.44	83.33	83.95
Coupled	q^{US}_{Guyton}	DM	0.67	0.31	0.55	−0.04 (0.15)	80.00	54.55	91.67	75.00	81.48
		PM	0.63	0.34	0.53	−0.04 (0.15)	78.10	48.48	91.67	72.73	79.52
		TAG	0.87	0.11	0.61	−0.01 (0.16)	86.67	78.79	90.28	78.79	90.28
	$q^{DeSimone}_{Guyton}$	DM	0.76	0.22	0.54	−0.02 (0.17)	82.86	66.67	90.28	75.86	85.53
		PM	0.70	0.26	0.52	−0.01 (0.16)	81.90	63.64	90.28	75.00	84.42
		TAG	0.95	0.02	0.61	0.02 (0.17)	85.71	78.79	88.89	76.47	90.14
	$\bar{q}^{US}_{Guyton}$	DM	0.70	0.29	0.54	−0.04 (0.15)	80.95	57.58	91.67	76.00	82.50
		PM	0.65	0.32	0.53	−0.04 (0.15)	77.14	42.42	93.06	73.68	77.91
		TAG	0.91	0.08	0.61	−0.00 (0.16)	88.57	78.79	93.06	83.87	90.54
	$q_{Sakamoto}$	DM	0.78	0.20	0.55	−0.02 (0.16)	82.86	66.67	90.28	75.86	85.53
		PM	0.73	0.24	0.54	−0.01 (0.16)	80.95	60.61	90.28	74.07	83.33
		TAG	0.98	0.00	0.63	0.02 (0.17)	83.81	78.79	86.11	72.22	89.86
	$\hat{q}_{Kishi}$	DM	0.68	0.30	0.55	−0.04 (0.15)	82.86	63.64	91.67	77.78	84.62
		PM	0.63	0.34	0.51	−0.03 (0.15)	81.90	57.58	93.06	79.17	82.72
		TAG	0.88	0.10	0.60	−0.00 (0.16)	87.62	78.79	91.67	81.25	90.41
	$\hat{q}_{Sharma}$	DM	0.70	0.28	0.54	−0.03 (0.15)	82.86	63.64	91.67	77.78	84.62
		PM	0.64	0.32	0.51	−0.03 (0.16)	79.05	54.55	90.28	72.00	81.25
		TAG	0.88	0.09	0.59	0.00 (0.16)	87.62	78.79	91.67	81.25	90.41

Note. For each column representing different accuracy measures, we have highlighted the best (green), second best (blue), and third best (red) measures. *a* and *b* are coefficients for linear fitting: $FFR_{RO}=a\,FFR_m+b$, while *r* is Pearson correlation coefficient.

Abbreviation: DM, distal Murray; FFR, fractional flow reserve; PM, proximal Murray; TAG, transluminal attenuation gradient.

TABLE 12 Comparison of FFR_{RO} vs FFR_m for different coronary segments. The rest of the settings are: coupled branches treatment and $\bar{q}^{US}_{Guyton}$ baseline flow

Coronary segments	Flow Distribution	a	b	r	$FFR_{RO}-FFR_m$	Acc.	Sen.	Spe.	PPV	NPV
All	DM	0.70	0.29	0.54	−0.04 (0.15)	80.95	57.58	91.67	76.00	82.50
	PM	0.65	0.32	0.53	−0.04 (0.15)	77.14	42.42	93.06	73.68	77.91
	TAG	0.91	0.08	0.61	−0.00 (0.16)	88.57	78.79	93.06	83.87	90.54
LAD	DM	0.72	0.29	0.56	−0.06 (0.15)	80.70	57.14	94.44	85.71	79.07
	PM	0.74	0.27	0.60	−0.06 (0.14)	77.19	38.10	100.00	100.00	73.47
	TAG	1.02	−0.01	0.70	−0.01 (0.14)	91.23	80.95	97.22	94.44	89.74
LCX	DM	0.58	0.34	0.44	−0.00 (0.21)	71.43	57.14	78.57	57.14	78.57
	PM	0.38	0.51	0.32	−0.02 (0.22)	66.67	42.86	78.57	50.00	73.33
	TAG	0.73	0.17	0.46	0.05 (0.25)	76.19	85.71	71.43	60.00	90.91
RCA	DM	0.90	0.11	0.72	−0.03 (0.08)	88.46	60.00	95.24	75.00	90.91
	PM	1.11	−0.10	0.75	0.01 (0.09)	84.62	60.00	90.48	60.00	90.48
	TAG	0.54	0.43	0.55	−0.03 (0.08)	92.31	60.00	100.00	100.00	91.30

Note. For each column representing different accuracy measures, we have highlighted the best (green), second best (blue), and third best (red) measures. *a* and *b* are coefficients for linear fitting: $FFR_{RO}=a\,FFR_m+b$, while *r* is Pearson correlation coefficient.

Abbreviation: DM, distal Murray; FFR, fractional flow reserve; PM, proximal Murray; TAG, transluminal attenuation gradient.

4.2 | Validation of reduced-order model

Validation of the reduced-order model using a 3D model as reference is significantly more extensive than previously published results. In Fossan et al,[19] an earlier version of the reduced-order model described here was validated on a population of 13 patients and 23 FFR measurements for a single flow configuration. Moreover, in Blanco et al,[17] a population of 20 patients and 32 FFR measurements for a single flow configuration was considered. Here, we consider 63 patients, 105 FFR measurements, and three different flow configurations.

Results depicted in Figure 3 show that the agreement between predicted FFR values by both models is satisfactory, as confirmed by results reported in Table 8. It is worth noting that the presented results allow to make a two-fold assessment of the reduced-order model results. On one hand, while using resistive elements at terminals, we can see how the entire modelling pipeline described in Section 2.4 is affected by using a simpler and computationally cheaper model with respect to using the 3D model. On the other hand, by imposing terminal flows from the results obtained using

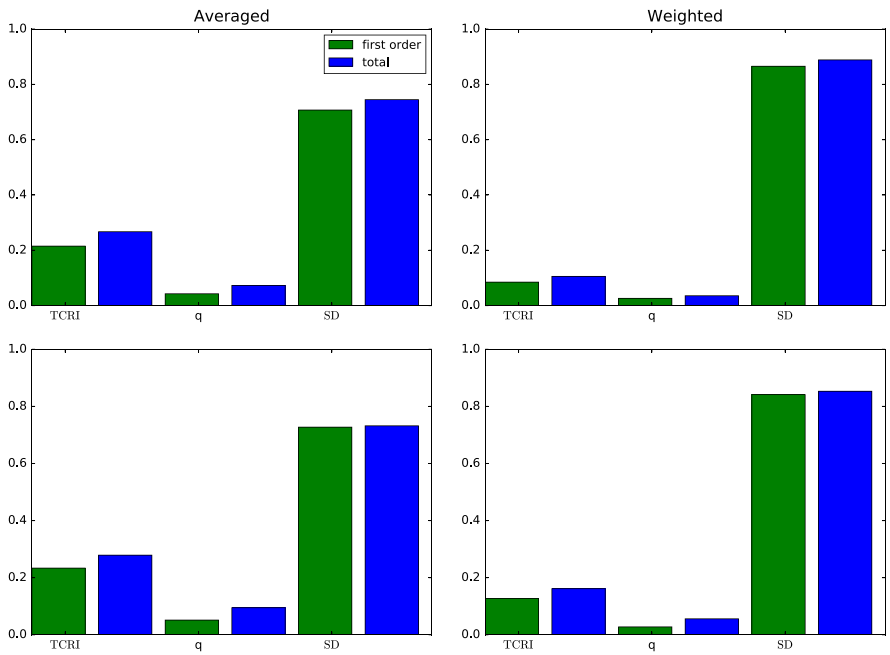

FIGURE 5 The average first-order and total sensitivity indices. The top two bar plots represent sensitivities when all 105 cases were considered, whereas in the bottom two, only cases (N=37) where fractional flow reserve (FFR) is in the critical region $0.7<FFR_{RO}<0.9$ are considered

the 3D model, we can focus on how well the reduced-order model reproduces pressure drops for fixed flows. As it can be clearly seen, the mismatch between results obtained using both models are larger in the case of prescribed flows at outlets of the reduced-order model. Consequently, this is the case where the benefits obtained by modifications to the original model proposed in Fossan et al[19] can be better observed. Furthermore, results reported in Table 9 show that predicted FFR deviations of the reduced-order model with respect to FFR predicted with the 3D model are small compared with errors in FFR prediction versus invasive measurements with bias (standard deviation) of −0.01 (0.03) and −0.05 (0.13) for FFR_{3D} versus FFR_{RO} and FFR_m versus FFR_{RO}, respectively. Importantly, when comparing diagnostic accuracy indexes for reduced-order and 3D model predicted FFR versus invasive measurements, one can see that these are only marginally affected by the used model. These considerations allow us to conclude that results discussed in the following sections are mostly affected by the different modelling hypotheses used (boundary conditions) and not by errors in the description of the fluid mechanics introduced by the reduced-order model. Nevertheless, we note that the disagreement between reduced-order model results and 3D model results leaves room for further reduced-order model improvement, as discussed in Section 4.5.

4.3 | Baseline coronary flow and FFR prediction by different strategies

4.3.1 | Predicted baseline coronary flow

When comparing FFR predictions by different model setups made in Section 3.3, we have excluded results obtained using baseline coronary flows q_{Sharma} and q_{Kishi}. The reason for this choice can be inferred from average baseline coronary flows reported in Table 10. In fact, predicted average flows for q_{Sharma} and q_{Kishi}, as well as average myocardium perfusion rate for q_{Sharma}, are well below physiological values of 250 mL/min and 0.8 mL/g/min.[34] Moreover, it is remarkable how these quantities are in line with reference values for methods using relation (14) to compute TMM and where flow is not derived from perfusion rates, ie, q^{US}_{Guyton}, $q^{DeSimone}_{Guyton}$, $q_{Sakamoto}$, and $\hat{q}_{Sharma}$.

4.3.2 | Effect of baseline coronary flow and its distribution on FFR prediction

Results presented in Table 11 clearly show that the flow distribution strategy for which our reduced-order model delivers better agreement with invasive measurements is the one based on TAG. In fact, linear fit coefficients and Pearson correlation coefficient are always better for TAG for fixed branch treatment and baseline flow estimation strategy. A closer look into how flow distribution methods effect FFR prediction on a vessel basis can be done from data shown in Table 12. Here, it becomes evident that TAG outperforms other flow distribution strategies for LAD and LCX but not for RCA. The overall better performance is due to the fact that lesions located in LAD and LCX (and their branches) account for almost 83 % of total lesion number, in combination with the fact that TAG systematically results in more blood flowing into the LAD with respect to flows obtained with DM and Proximal Murray (PM). For example, for coupled branches treatment and $\bar{q}^{US}_{Guyton}$, average (standard deviation) flow in the LAD are 74 (26), 71 (26), and 89 (32)mL/min for DM, PM, and TAG flow distribution strategies, respectively. Such a pattern can be observed for all simulations reported in Table 11. The larger flow can compensate for underestimated stenosis severity or it can simply mean that TAG is better reflecting the flow distribution among vessels. This last observation is supported by the fact that TAG incorporates patient-specific information about flow distribution (via intensity gradients along vessels), while DM and PM are based on geometrical information alone.

The best performing method in terms of correlation to invasive measurements has the following setting: coupled branches treatment, $q_{Sakamoto}$, and TAG flow distribution. On the other hand, the best method in terms of diagnostic accuracy has the following setting: coupled branches treatment, $\bar{q}^{US}_{Guyton}$, and TAG flow distribution. Since this last method ranks second in terms of linear fitting coefficients, we will denote it as FFR^{OPT}_{RO} throughout the rest of this work.

Diagnostic performance for different modelling choices can vary significantly. In particular, sensitivity among explored model setups varies between 48.48% and 78.79%. It is interesting to observe that maximum sensitivity (78.79%) is achieved for coupled branches treatment, TAG flow distribution, and all baseline coronary flow estimation methods, pointing out to the fact that flow distribution is more determinant than baseline coronary flow estimation.

Although errors ($FFR_{RO}-FFR_m$) standard deviation varies for different model setups, such fluctuations are very small with respect to standard deviation absolute values, with larger variations among results obtained using different baseline flow definition methods rather than within single baseline flow definition methods. In other words, standard

TABLE 13 Comparison of FFR_{RO} vs FFR_m for different ways of estimating the proximal boundary condition. The rest of the settings are coupled branches treatment, $\bar{q}^{US}_{Guyton}$ baseline flow, and TAG flow distribution

Inlet pressure	*a*	*b*	*r*	$FFR_{RO}-FFR_m$	Acc.	Sen.	Spe.	PPV	NPV
Clinic	1.03	−0.03	0.65	0.00 (0.16)	89.47	79.31	93.94	85.19	91.18
100	1.02	−0.02	0.65	0.00 (0.16)	88.42	79.31	92.42	82.14	91.04
Invasive	1.04	−0.04	0.66	0.00 (0.16)	88.42	79.31	92.42	82.14	91.04

[a]: FFR, fractional flow reserve; TAG, transluminal attenuation gradient.

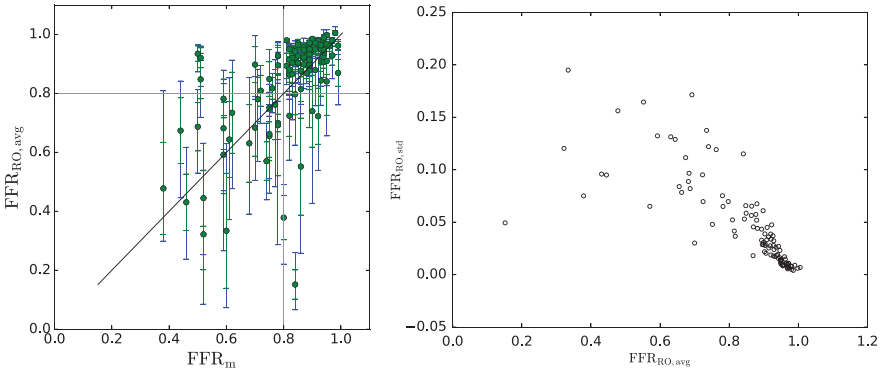

FIGURE 6 Left panel shows a scatter plot of $FFR_{RO,avg}$ vs FFR_m, where $FFR_{RO,avg}$ is the average FFR predicted from the simulations summarised in Table 11. The range (blue) of predicted FFR_{RO} and standard deviation, $FFR_{RO,std}$ (green) are also indicated by the vertical error bars. Right panel shows $FFR_{RO,std}$ as a function of $FFR_{RO,avg}$

deviation changes seem to be mainly due to the use of different baseline flow estimation methods, rather than by flow distribution strategies. Another conclusion that can be made from standard deviation variation across used modelling setups is that none of the investigated methods seems to reduce error standard deviation significantly, although several of them imply using patient-specific information. This result is not surprising if one considers the origin of patient-specific information used by the different methods. In q^{US}_{Guyton}, we use ultrasound-derived CO, for which measurement errors of 690mL/min have been reported. Such errors propagate to baseline coronary flow, which, in this case, is computed as 4.5 % of CO and imply an error in flow of approximately 31 mL/min or 14 % of baseline coronary flow. The standard deviation of q^{US}_{Guyton} in our population is 42 mL/min and is thus comparable with the measurement error. Another method using CO estimates is $q^{DeSimone}_{Guyton}$, where the formula for determining stroke volume (7) was obtained by fitting experimental data, with a resulting Pearson correlation coefficient r=0.45, [33] denoting large uncertainty in predicted values. Moving forward among methods, we consider now $\hat{q}_{Sharma}$. In this case, (13) is used. This relation involves a fitting of experimental data (on dogs) relating HR and SBP to oxygen consumption, with r=0.87, [51] combined then to another fitting of experimental data on the relation between coronary flow and oxygen consumption.[52] There are additional sources of errors for these patient-specific baseline flow estimation methods. The fraction of CO that flows into the coronaries, γ in (10), is assumed constant. Moreover, as already discussed, some methods make use of SBP and HR. These quantities are known to vary for the same patient depending on many factors. For our patient population, we observe that Pearson correlation coefficients for SBP and HR when comparing quantities acquired non-invasively and quantities measured during invasive FFR procedures are 0.09 and 0.29, for SBP and HR, respectively. All these considerations support the results shown here that evidence no benefit in terms of error standard deviation reduction by using patient-specific baseline flow estimation methods. However, this conclusion does not preclude that a better, currently nonreported baseline flow estimation method would result in improved FFR predictions.

Previously reported relative low impact of prescribed inlet pressure in FFR prediction frameworks[19,21] was confirmed in this study. Table 13 shows the completely neglectable impact of using different values for the prescribed inlet pressure, including pressure measured non-invasively, pressure acquired during invasive FFR measurement (the actual value to compute invasive FFR), and a fixed value of 100 mmHg, demonstrating that this parameter is of little importance when predicting FFR.

Figure 6, left panel, shows a scatter plot of invasive FFR versus average predicted FFR (for all methods shown in Table 11), including maximum variation ranges and standard deviation. Average standard deviation is 0.048, with larger values for lower FFR values, as it can be seen in Figure 6, right panel. These results reinforce observations made while analysing data reported in Table 11 on the fact that baseline coronary flow estimation and flow distribution strategies

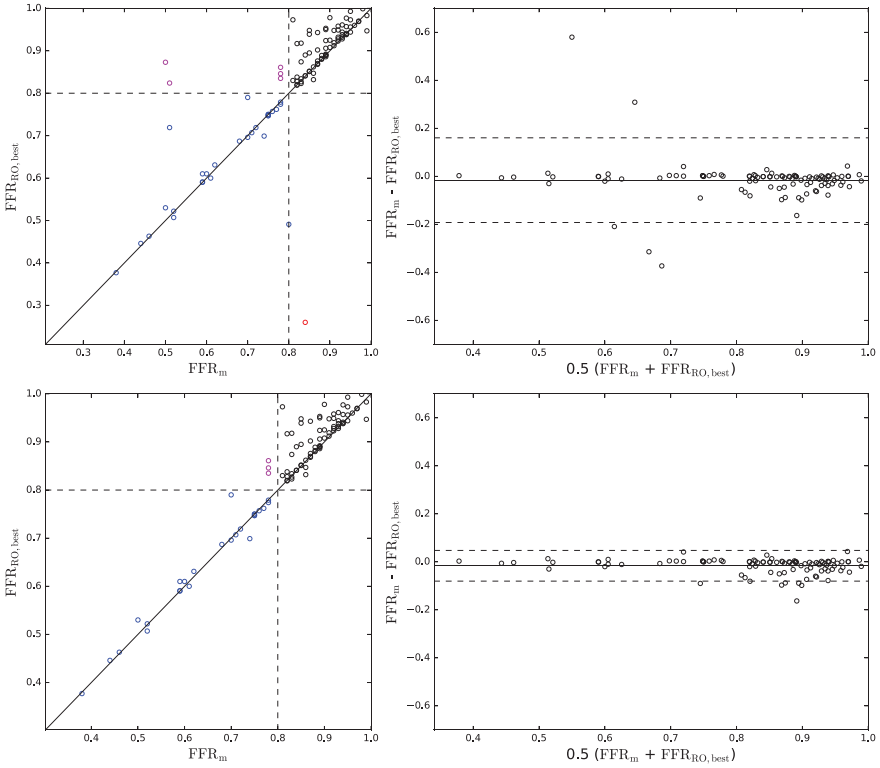

FIGURE 7 Scatter plot and Blant-Altman of $FFR_{RO,best}$ vs FFR_m, where FFR_{best} is the best FFR prediction (in terms of absolute error) from all the simulations summarised in Table 11. The top panel shows results when all measurements are included, whereas those in the bottom row (5) measurements which had errors ($FFR_{RO,best}-FFR_m$) larger than two standard deviations were excluded. $FFR_{RO,best}-FFR_m$ are −0.02 (0.09) and −0.02 (0.03) for the top and bottom panels, respectively. FFR, fractional flow reserve

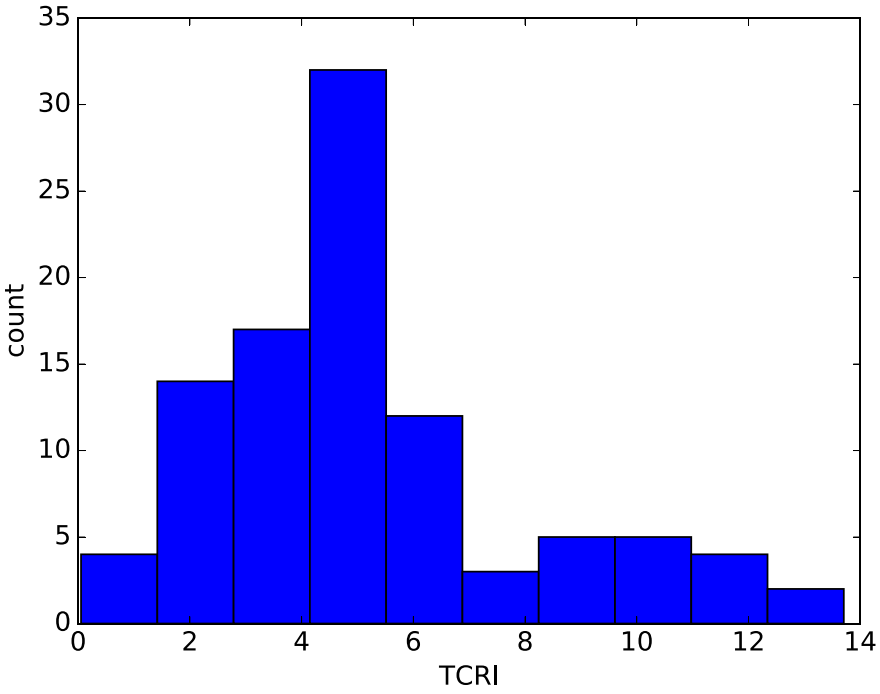

FIGURE 8 Histogram of TCRI, where TCRI in this case is calculated on the basis of the baseline resistance of simulations corresponding to the best performing setting (coupled branches treatment, $\bar{q}^{US}_{Guyton}$ baseline flow, and TAG flow distribution) and hyperemic resistance corresponding to FFR_{best}. Measurement locations which had errors ($FFR_{RO,best}-FFR_m$) larger than two standard deviations where excluded and cases which resulted in TCRI values larger than 15 were excluded from this analyses. FFR, fractional flow reserve; TCRI, total coronary resistance index

have limited impact on overall performance of the FFR prediction framework: Average of predicted FFR standard deviation to baseline flow and flow distribution methods is 0.048 while predicted FFR measurement error standard deviation is 0.15. This fact indicates that the availability of better baseline flow estimation and flow distribution methods will have a significant but limited impact on FFR prediction performance. Such impact can increase if one considers that the precise definition of one of the parameters with larger impact on FFR predictions, the TCRI,[19,21] depends on a baseline condition. These findings are further supported by our sensitivity analysis, where we see that the effect of the uncertainty in baseline coronary flow is rather low, compared with the influence of TCRI and SD. Results indicate

that the uncertainty in the stenosis degree has the largest influence on FFR-prediction uncertainty, with average first-order and total sensitivity indices of 0.71 and 0.74, and uncertainty weighted sensitivity indices of 0.87 and 0.89, respectively. TCRI has a significant but much lower influence with average first-order and total sensitivity indices of 0.22 and 0.27 and uncertainty weighted sensitivity indices of 0.08 and 0.11, respectively. Baseline coronary flow has a minor influence in comparison, with average first order and total sensitivity indices of 0.04 and 0.07 and uncertainty weighted sensitivity indices of 0.03 and 0.04, respectively. The influence of TCRI and q is slightly increased when only cases in the critical region $0.7<FFR_{\mathrm{RO}}<0.9$ are considered. The average standard deviation in predicted FFR is 0.12. However, we note that the uncertainty in how the flow is distributed is not considered and may be seen in relation to the fact that the average standard deviation resulting from the UQ&SA (0.12) is slightly lower than average predicted FFR measurement error standard deviation (0.15).

The above made observations allow us to conclude that other parameters than the ones studied here have to be addressed in order to improve FFR prediction accuracy. In particular, we consider now TCRI and make a post-processing experiment by:

- extracting best matching FFR predictions of all simulations shown in Table 11;
- considering $\mathrm{FFR}_{\mathrm{RO}}^{\mathrm{OPT}}$ as the setting for reference baseline conditions; and
- compute TCRI as the ratio of peripheral resistance (with respect to FFR measurement location) for best matching simulation versus peripheral resistance for reference baseline setting.

Selected best matching predictions versus measurements are shown in Figure 7, while Figure 8 shows a histogram of obtained TCRIs. Such results show that, for the given modelling framework, available segmentations and flows in physiological ranges, rather accurate FFR predictions can be obtained, if a highly variable TCRI is considered. Corresponding accuracy, sensitivity, and specificity are 94%, 85%, and 99% when all measurements are included and 97%, 90%, and 100% when outliers are excluded. Interestingly, TCRI distribution emerging from this analysis reflects the high variability observed in coronary flow reserve, which has shown to display a gamma distribution shape when directly measured on patients.[53]

4.4 | Use of reduced-order models for the development of clinical decision support tools

The capacity of exploring a large number of modelling hypotheses, as well as parameter space via sensitivity analysis, is facilitated by the fact that we use an accurate reduced-order model of the problem under investigation. This fact points to one of the strengths of reduced-order models, which is that of being computationally cheaper and generally more robust than more complex models in terms of numerical issues such as convergence and stability of the overall algorithm. Advantages in terms of problem setup, preprocessing, and postprocessing over more complex models are also relevant. Moreover, errors introduced by reduced-order models can be compensated by the fact that one can explore a larger portion of possible solutions. However, such errors must be acceptable, which in the context of this work means that clinical decisions should not be affected by them.

4.5 | Limitations and future work

The present work has several limitations. The most relevant one is probably the fact that, although we explore certain modelling hypotheses, other are kept fixed and are inherent to our FFR prediction framework (segmentation method, modelling pipeline, etc). This fact is kept in mind throughout the text and only claims that we think are valid for any model-based FFR prediction framework are mentioned as such. The impact of patient-specific TCRI on FFR prediction diagnostic accuracy was only partially addressed. In fact, in Section 4.3.2 we show that a highly variable TCRI would have a significant impact in the diagnostic accuracy of our FFR prediction method. Ideally, we should assess how a patient-specific TCRI computation would perform in comparison to other methods, but to the best of our knowledge, no methodology to estimate TCRI non-invasively and without the use of drugs or additional imaging is currently available. Another component that can vary greatly among patients is total baseline coronary flow. In this case, we have considered quantification methods that depend on patient-specific information such as CO or LVM. However, one should ideally use a direct total baseline coronary flow measurement method. Such methods are being developed in the context of ultrasound imaging and magnetic resonance imaging and, once available, have the potential to provide

highly valuable information for FFR prediction tools. See Fiorentini et al[54] and Schwitter et al[55] for recent developments in ultrasound and magnetic-resonance coronary flow estimation methods.

Another aspect to be considered is the fact that the reduced-order model is not perfectly reproducing 3D model results. Therefore, results are influenced not only by boundary conditions but also by errors in solving fluid mechanics within the computational domain representing epicardial vessels. This is common to any FFR prediction strategy based on reduced-order models. Here, we prefer to be aware of such errors and try to minimise them, rather than to embed them in the modelling framework and lose control on error causes when comparing FFR prediction and invasive measurements.

The prevalence of positive FFR values is not optimal, and one would desire a more homogeneous distribution of invasive FFR values to work with. However, we observe that this is an issue faced by virtually all published works on FFR prediction methods and is probably related to the intrinsic dynamics of how FFR is used in the clinic, with many measurements performed on lesions that reveal to be functionally nonsignificant.

Finally, the results from the UQ & SA depend on the assumed input uncertainties, and here we did not include uncertainties/variability due to differences in how baseline coronary flow is distributed. More importantly, the way in which the uncertainty of the stenosis geometry was modelled, via a global parameter effecting all stenotic regions, may have synthetically increased the influence of this parameter and is not necessarily entirely realistic. Nevertheless, results shown here should still be considered as valid for giving a clear indication to where attention should be focused in order to reduce uncertainty in FFR-prediction.

4.6 | Conclusions and future work

In this work, we have first improved and validated a reduced-order model for FFR prediction and then tested the impact of different methods proposed in the literature to estimate and distribute baseline coronary flow on FFR predictions. Both tasks were performed on a dataset regarding 63 patients with stable CAD and 105 invasive FFR measurements.

The proposed reduced-order model introduces errors with respect to the 3D model, which are significantly smaller than errors observed for predicted FFR versus invasive measurements. Moreover, diagnostic performance was only marginally affected by the use of the reduced-order model for cases in which 3D simulation results were available (63 patients, 105 invasive FFR measurements, 3 different setups for 3D simulations).

We have shown that methods for baseline coronary flow estimation and its distribution can affect the diagnostic performance of an FFR-prediction framework significantly. Moreover, the influence of methods for flow distribution is greater than that of methods for baseline flow estimation, and we find that TAG flow distribution outperforms flow distribution methods based on Murray's law for all tested setups. However, we observe that none of the investigated methods for baseline coronary flow estimation and distribution results in a significant reduction in error standard deviation for predicted FFR versus invasive FFR measurements. Finally, we see that for our modelling framework the diagnostic accuracy on a per-vessel basis can vary significantly.

In future work, we will regard the further improvement of our reduced-order model in terms of its capacity to reproduce the physics of 3D models in a more accurate manner. Moreover, we will look into better ways of characterising baseline coronary flow by means of, for example, non-invasive determination of baseline flow at selected vessels. Finally, we will consider how to better define a patient-specific TCRI, since we think that this factor plays a crucial role in representing patient-specific variability in coronary physiology relevant for FFR prediction.

ACKNOWLEDGEMENTS

This work was partially supported by NTNU Health (Strategic Research Area at the Norwegian University of Science and Technology) and by The Liaison Committee for education, research, and innovation in Central Norway. Computational resources in Norwegian HPC infrastructure were granted by the Norwegian Research Council by Project Nr. NN9545K.

ETHICAL APPROVAL

All procedures performed in studies involving human participants were in accordance with the ethical standards of the institutional and/or national research committee and with the 1964 Helsinki declaration and its later amendments or comparable ethical standards.

ORCID

Fredrik E. Fossan https://orcid.org/0000-0003-0006-5165

REFERENCES

1. Pijls NHJ, Van Gelder B, Van der Voort P, et al. A useful index to evaluate the influence of an epicardial coronary stenosis on myocardial blood flow. *Circulation*. 1995;92(11):3183-3193. https://doi.org/10.1161/01.CIR.92.11.3183
2. Pijls NH, De Bruyne B, Peels K, et al. Measurement of fractional flow reserve to assess the functional severity of coronary-artery stenoses. *N Engl J Med*. 1996;334(26):1703=-1708.
3. Pijls NH, Van Son JA, Kirkeeide R, De Bruyne B, Gould KL. Experimental basis of determining maximum coronary, myocardial, and collateral blood flow by pressure measurements for assessing functional stenosis severity before and after percutaneous transluminal coronary angioplasty. *Circulation*. 1993;87(4):1354-1367.
4. Wilson RF, Wyche K, Christensen BV, Zimmer S, Laxson DD. Effects of adenosine on human coronary arterial circulation. *Circulation*. 1990;82(5):1595-1606. https://doi.org/10.1161/01.CIR.82.5.1595
5. Tonino PA, De Bruyne B, Pijls NH, et al. Fractional flow reserve versus angiography for guiding percutaneous coronary intervention. *N Engl J Med*. 2009;360(3):213-224.
6. Pijls NH, Fearon WF, Tonino PA, et al. Fractional flow reserve versus angiography for guiding percutaneous coronary intervention in patients with multivessel coronary artery disease. *J Am Coll Cardiol*. 2010;56(3):177-184. https://doi.org/10.1016/j.jacc.2010.04.012
7. De Bruyne B, Pijls NH, Kalesan B, et al. Fractional flow reserve-guided PCI versus medical therapy in stable coronary disease. *N Engl J Med*. 2012;367(11):991-1001. https://doi.org/10.1056/NEJMoa1205361
8. 2014 ESC/EACTS Guidelines on myocardial revascularization: The Task Force on Myocardial Revascularization of the European Society of Cardiology (ESC) and the European Association for Cardio-Thoracic Surgery (EACTS)Developed with the special contribution of the European Association of Percutaneous Cardiovascular Interventions (EAPCI). *Eur Heart J*. 2014;35(37):2541-2619. https://doi.org/10.1093/eurheartj/ehu278
9. Patel MR, Peterson ED, Dai D, et al. Low diagnostic yield of elective coronary angiography. *N Engl J Med*. 2010;362(10):886-895. https://doi.org/10.1056/NEJMoa0907272
10. The SCOT-HEART Investigators. Coronary CT angiography and 5-year risk of myocardial Infarction. *N Engl J Med*. 2018;379(10):924-933. https://doi.org/10.1056/NEJMoa1805971
11. NICE. National Institute for Health and care excellence clinical guideline on chest pain of recent onset: assessment and diagnosis; 2010.
12. Rossi A, Papadopoulou SL, Pugliese F, et al. Quantitative computed tomographic coronary angiography: does it predict functionally significant coronary stenoses? *Circ Cardiovasc Imaging*. 2014;7(1):43-51. https://doi.org/10.1161/CIRCIMAGING.112.00027
13. Cook CM, Petraco R, Shun-Shin MJ, et al. Diagnostic accuracy of computed tomography-derived fractional flow reserve: a systematic review. *JAMA Cardiol*. 2017;2(7):803–810. https://doi.org/10.1001/jamacardio.2017.1314
14. Nørgaard BL, Terkelsen CJ, Mathiassen ON, et al. Clinical outcomes using coronary CT angiography and FFRCT guided management of stable chest pain patients. *J Am Coll Cardiol*; 2018;72(18):2123–2134. https://doi.org/10.1016/j.jacc.2018.07.043
15. Itu L, Sharma P, Mihalef V, Kamen A, Suciu C, Lomaniciu D. A patient-specific reduced-order model for coronary circulation. *IEEE*. 2012;■:832-835.
16. Ri K, Kumamaru KK, Fujimoto S, et al. Noninvasive computed tomography-derived fractional flow reserve based on structural and fluid analysis: reproducibility of on-site determination by unexperienced observers. *J Comput Assist Tomogr*. 2017;42(2):256–262. https://doi.org/10.1097/RCT.0000000000000679
17. Blanco PJ, Bulant CA, Müller LO, et al. Comparison of 1D and 3D models for the estimation of fractional flow reserve. *Sci Rep*. 2018;8(1). https://doi.org/10.1038/s41598-018-35344-0
18. Boileau E, Pant S, Roobottom C, et al. Estimating the accuracy of a reduced-order model for the calculation of fractional flow reserve (FFR). *Int J Numer Methods Biomed Eng*. 2018;34(1):e2908. https://doi.org/10.1002/cnm.2908
19. Fossan FE, Sturdy J, Müller LO, et al. Uncertainty quantification and sensitivity analysis for computational FFR estimation in stable coronary artery disease. *Cardiovasc Eng Technol*. 2018;9(4):597–622. https://doi.org/10.1007/s13239-018-00388-w
20. Sankaran S, Kim HJ, Choi G, Taylor CA. Uncertainty quantification in coronary blood flow simulations: impact of geometry, boundary conditions and blood viscosity. *J Biomech*; 2016;49(12):2540-2547. https://doi.org/10.1016/j.jbiomech.2016.01.002
21. Morris PD, Soto DAS, Feher JFA, et al. Fast virtual fractional flow reserve based upon steady-state computational fluid dynamics analysis. *JACC Basic Trans Sci*. 2017;2(4):434-446. https://doi.org/10.1016/j.jacbts.2017.04.003
22. Bråten AT, Wiseth R. Diagnostic accuracy of CT-FFR compared to invasive coronar angiography with fractional flow reserve - full text view - ClinicalTrials. gov; 2017.
23. Gaur S, Øvrehus KA, Dey D, et al. Coronary plaque quantification and fractional flow reserve by coronary computed tomography angiography identify ischaemia-causing lesions. *Eur Heart J*. 2016;37(15):1220-1227. https://doi.org/10.1093/eurheartj/ehv690

24. Yushkevich PA, Piven J, Hazlett HC, Smith RG, Ho S, Gee JC, Gerig G. User-guided 3D active contour segmentation of anatomical structures: significantly improved efficiency and reliability. *NeuroImage*. 2006;31(3):1116-1128. https://doi.org/10.1016/j.neuroimage.2006.01.015
25. Antiga L, Piccinelli M, Botti L, Ene-Iordache B, Remuzzi A, Steinman DA. An image-based modeling framework for patient-specific computational hemodynamics. *Medical & Biological Engineering & Computing*. 2008;46(11):1097-1112. https://doi.org/10.1007/s11517-008-0420-1
26. Srl O. The vascular modeling toolkit website; Accessed: 2017.
27. Seeley BD, Young DF. Effect of geometry on pressure losses across models of arterial stenoses. *J Biomech*. 1976;9(7):439-448. https://doi.org/10.1016/0021-9290(76)90086-5
28. Evju Ø, Alnæs MS. CBCFLOW. Bitbucket repository; 2017.
29. Logg A, Mardal KA, Wells G, eds.. *Automated Solution of Differential Equations by the Finite Element Method. 84 of Lecture Notes in Computational Science and Engineering*. Berlin, Heidelberg: Springer Berlin Heidelberg; 2012.
30. Simo JC, Armero F. Unconditional stability and long-term behavior of transient algorithms for the incompressible Navier-Stokes and Euler equations. *Computer Methods in Applied Mechanics and Engineering*. 1994;111(1–2):111-154. https://doi.org/10.1016/0045-7825(94)90042-6
31. Mortensen M, Valen-Sendstad K. A high-level/high-performance open source Navier-Stokes solver. *Comput Phys Commun*. 2015;188:177-188. https://doi.org/10.1016/j.cpc.2014.10.026
32. Bezerra CG, Hideo-Kajita A, Bulant CA, et al. Coronary fractional flow reserve derived from intravascular ultrasound imaging: validation of a new computational method of fusion between anatomy and physiology. *Catheter Cardiovasc Interv*. 2019;93(2):266-274. https://doi.org/10.1002/ccd.27822
33. de Simone G, Roman MJ, Koren MJ, Mensah GA, Ganau A, Devereux RB. Stroke volume/pulse pressure ratio and cardiovascular risk in arterial hypertension. *Hypertens*. 1999;33(3):800-805. https://doi.org/10.1161/01.HYP.33.3.800
34. Guyton AC, Hall JE. *Textbook of Medical Physiology*. 11th. Philadelphia: Elsevier Saunders; 2006.
35. Kishi S, Giannopoulos AA, Tang A, et al. A framework for personalization of coronary flow computations during rest and hyperemia. *Radiol*. 2017;■:162620. https://doi.org/10.1148/radiol.2017162620
36. Zipes DP, Libby P, Bonow RO, Mann DL, Tomaselli GF, Braunwald E. Braunwald's heart disease: a textbook of cardiovascular medicine. OCLC: 1021152059; 2019.
37. Sharma P, Itu L, Zheng X, et al. A framework for personalization of coronary flow computations during rest and hyperemia. IEEE; 2012:6665-6668.
38. Molina DK, DiMaio VJ. Normal organ weights in men: part I—the heart. *Am J Forensic Med Pathol*. 2012;33(4):362-367. https://doi.org/10.1097/PAF.0b013e31823d298b
39. Molina DK, DiMaio VJ. Normal organ weights in men: part I—the heart. *Am J Forensic Med Pathol*. 2015;36(3):176-181. https://doi.org/10.1097/PAF.0000000000000174
40. Sakamoto S, Takahashi S, Coskun AU, et al. Relation of distribution of coronary blood flow volume to coronary artery dominance. *Am J Cardiol*. 2013;111(10):1420-1424. https://doi.org/10.1016/j.amjcard.2013.01.290
41. Murray CD. The physiological principle of minimum work. *Proc Natl Acad Sci USA*. 1926;12(3):207-214.
42. Taylor CA, Fonte TA, Min JK. Computational fluid dynamics applied to cardiac computed tomography for noninvasive quantification of fractional flow reserve. *J Am Coll Cardiol*. 2013;61(22):2233-2241. https://doi.org/10.1016/j.jacc.2012.11.083
43. Bulant CA. Computational models for the geometric and functional analysis of the coronary circulation. *PhD Thesis*; 2017.
44. Saltelli Andrea. *Global Sensitivity Analysis : The Primer*. Chichester, England: John Wiley,; 2008.
45. Eck VG, Sturdy J, Hellevik LR. Effects of arterial wall models and measurement uncertainties on cardiovascular model predictions. *J Biomech*. 2016;50:188–194. https://doi.org/doi:10.1016/j.jbiomech.2016.11.042
46. Saltelli A. Making best use of model evaluations to compute sensitivity indices. *Comput Phys Commun*. 2002;145(2):280-297.
47. Robert C, Casella G. *Monte Carlo Statistical Methods*. 2nd ed. Springer-Verlag New York: Springer; 2004.
48. Fuchs A, Mejdahl MR, Kühl JT, et al. Normal values of left ventricular mass and cardiac chamber volumes assessed by 320-detector computed tomography angiography in the Copenhagen General Population Study. *European Heart Journal – Cardiovascular Imaging*. 2016;17(9):1009-1017. https://doi.org/10.1093/ehjci/jev337
49. Ang D, Pringle S, Struthers A. The cardiovascular risk factor, left ventricular hypertrophy, is highly prevalent in stable, treated angina pectoris. *Am J Hypertens*. 2007;20(10):1029-1035. https://doi.org/10.1016/j.amjhyper.2007.04.021
50. Abdi-Ali A, Miller RJH, Southern D, et al. LV mass independently predicts mortality and need for future revascularization in patients undergoing diagnostic coronary angiography. *JACC Cardiovasc Imaging*. 2018;11(3):423-433. https://doi.org/10.1016/j.jcmg.2017.04.012
51. Baller D, Bretschneider HJ, Hellige G. Validity of myocardial oxygen consumption parameters. *Clin Cardiol*. 1979;2(5):317-327.
52. Rubio R, Berne RM. Regulation of coronary blood flow. *Prog Cardiovasc Dis*. 1975;18(2):105-122. https://doi.org/10.1016/0033-0620(75)90001-8

53. Matsuda J, Murai T, Kanaji Y, et al. Prevalence and clinical significance of discordant changes in fractional and coronary flow reserve after elective percutaneous coronary intervention. *J Am Heart Assoc*. 2016;5(12). https://doi.org/10.1161/JAHA.116.004400

54. Fiorentini S, Saxhaug L, Bjåstad T., Holte E, Torp H, Avdal J. 3D tracking Doppler for improved quantitative blood flow assessment of coronary arteries. *2017 IEEE International Ultrasonics Symposium (IUS)*. 2017;■:1-4.

55. Schwitter J, DeMarco T, Kneifel S, et al. Magnetic resonance-based assessment of global coronary flow and flow reserve and its relation to left ventricular functional parameters : a comparison with positron emission tomography. *Circulation*. 2000;101(23):2696-2702. https://doi.org/10.1161/01.CIR.101.23.2696

How to cite this article: Müller LO, Fossan FE, Bråten AT, Jørgensen A, Wiseth R, Hellevik LR. Impact of baseline coronary flow and its distribution on fractional flow reserve prediction. *Int J Numer Meth Biomed Engng*. 2019;e3246. https://doi.org/10.1002/cnm.3246